bioRxiv preprint doi: https://doi.org/10.1101/648477; this version posted May 24, 2019. The copyright holder for this preprint (which was not certified by peer review) is the author/funder. All rights reserved. No reuse allowed without permission.

Title: Neuronal hyperexcitability drives TDP43 pathology by upregulating shortened TDP43 protein isoforms

Key Words: TDP43, ALS, hyperexcitability, alternative splicing, TDP43 pathology, iPSC, iNeuron

Authors: Kaitlin Weskamp[1,2], Elizabeth M. Tank[1], Roberto Miguez[1], Nicolás B. Gómez[1,3], Matthew White[4], Zigiang Lin[4], Carmen Moreno Gonzalez[5], Andrea Serio[5], Jemeen Sreedharan[4], Sami J. Barmada[1,2,3,*]

Affiliations: [1]Department of Neurology, [2]Neuroscience Graduate Program, [3]Cellular and Molecular Biology Program, University of Michigan, Ann Arbor, MI, USA; [4]Department of Basic and Clinical Neuroscience, [5]Centre for Craniofacial and Regenerative Biology, King's College London, London, UK.

*** To whom correspondence should be addressed:**

Sami Barmada

University of Michigan, Department of Neurology

109 Zina Pitcher Place, BSRB 5015

Ann Arbor, MI 48109

sbarmada@umich.edu

Abstract

Cortical hyperexcitability and mislocalization of the RNA-binding protein TDP43 are highly-conserved features in amyotrophic lateral sclerosis (ALS). Nevertheless, the relationship between

bioRxiv preprint doi: https://doi.org/10.1101/648477; this version posted May 24, 2019. The copyright holder for this preprint (which was not certified by peer review) is the author/funder. All rights reserved. No reuse allowed without permission.

these phenomena remains poorly defined. Here, we show that hyperexcitability recapitulates TDP43 pathology by upregulating shortened (s) TDP43 splice isoforms. These truncated isoforms accumulate in the cytosol, where they form insoluble inclusions that sequester full-length TDP43 via preserved N-terminal interactions. Consistent with these findings, sTDP43 overexpression is toxic to mammalian neurons, suggesting that neurodegeneration results from complementary gain- and loss-of-function mechanisms. In humans and mice, sTDP43 transcripts are enriched in vulnerable motor neurons, and we observed a striking accumulation of sTDP43 within neurons and glia of ALS patients. These studies uncover a hitherto unknown role of alternative TDP43 isoforms in ALS, and indicate that sTDP43 production may be a key contributor to the susceptibility of motor neurons in ALS.

Introduction

Amyotrophic lateral sclerosis (ALS) is a neurodegenerative disorder in which the progressive loss of motor neurons results in paralysis and respiratory failure[1]. There is no disease-modifying therapy for ALS, and its heterogeneous biochemical, genetic, and clinical features complicate the identification of therapeutic targets. However, the cytoplasmic mislocalization and accumulation of TDP43 (TAR DNA-binding protein of 43 kD), a nuclear RNA-binding protein integrally involved in RNA metabolism, is observed in >90% of individuals with ALS[2]. Moreover, while mutations in the gene encoding TDP43 (*TARDBP*) only account for 2-5% of ALS cases, mutations in several other ALS-associated genes including *C9orf72*[3], *ANG*[4], *TBK1*[5], *PFN1*[6], *UBQLN2*[7], *VCP*[8], and *hnRNPA2/B1*[9] result in TDP43 pathology.

bioRxiv preprint doi: https://doi.org/10.1101/648477; this version posted May 24, 2019. The copyright holder for this preprint (which was not certified by peer review) is the author/funder. All rights reserved. No reuse allowed without permission.

TDP43 is an essential protein involved in several RNA processing events, including splicing, translation, and degradation. In keeping with these fundamental functions, TDP43 levels and localization are tightly regulated and critical for cell health. TDP43 knockout animals exhibit neurodegeneration and behavioral deficits[10–13], while TDP43 overexpression results in neurodegeneration in primary neuron[14,15], mouse[16,17], rat[18,19], Drosophila[20,21], zebrafish[22,23], and primate models[24,25]. Furthermore, mislocalization of TDP43 to the cytosol is sufficient to drive cell death[14]. Taken together, this suggests that even small changes to TDP43 levels and localization are highly predictive of neurodegeneration.

Hyperexcitability, or an increase in neuronal activity, is a second feature observed in both familial and sporadic ALS cases[26]. Cortical hyperexcitability precedes symptom onset in some cases[26], and the degree of motor neuron excitability is a strong predictor of disease progression[27,28]. Such hyperexcitability arises from a loss of cortical inhibition[26,29–33] in combination with intrinsic differences in channel expression, content, and activity within motor neurons themselves[26,28,34,35]. Emphasizing the contribution of hyperexcitability to disease, riluzole — one of two available therapies for ALS — is a sodium channel antagonist that partially rescues hyperexcitability[36]. Animal models of ALS recapitulate key features of hyperexcitability[37–39], including an increase in motor neuron activity that precedes the onset of motor deficits[37,39,40] and reduced activity following treatment with riluzole[41]. Hyperexcitability is also observed in iPSC-based ALS models[42,43], though other reports suggest that it is a transient or developmental phenomenon[43,44].

Despite the prevalence of both TDP43 pathology and hyperexcitability in ALS, the relationship between these phenomena remains poorly defined. Here, we utilize an iPSC-derived neuron (iNeuron) model system to demonstrate that hyperexcitability drives TDP43 pathology characteristic of ALS via the upregulation of atypical, shortened TDP43 isoforms. Using multiple model systems and human post-mortem material, we show that these unusual isoforms are exported from the nucleus, form insoluble cytosolic inclusions, are neurotoxic, and are enriched

bioRxiv preprint doi: https://doi.org/10.1101/648477; this version posted May 24, 2019. The copyright holder for this preprint (which was not certified by peer review) is the author/funder. All rights reserved. No reuse allowed without permission.

in ALS patient tissue, thereby directly implicating alternative TDP43 isoforms in ALS pathogenesis.

Results

TDP43 is regulated by neuronal activity

To investigate disease mechanisms related to hyperexcitability in human neurons, we established an induced pluripotent stem cell (iPSC) derived neuron (iNeuron) model. Transcription activator-like endonucleases (TALENs) specific for the *CLYBL* safe harbor locus were used to introduce the transcription factors Neurogenin 1 and 2 (Ngn1-2) under a doxycycline (dox)-inducible promoter (Figure 1A). Expression of Ngn1-2 is sufficient to drive the rapid differentiation of iPSCs into iNeurons that display immunocytochemical and electrophysiological properties of glutamatergic, excitatory forebrain-like neurons[45–47] (Figure 1B). Consistent with this, within 2 weeks of dox addition iNeurons adopt a neuronal morphology and stain positive for the neuronal markers Vglut1 and Tuj1 (Figure 1C). We further validated the maturity of neurons differentiated in this manner using an iPSC line that stably expresses the fluorescent calcium indicator gCaMP6f in addition to dox-inducible Ngn1-2[48]. Because time-dependent changes in gCaMP6f fluorescence correlate with action potentials, we monitored neuronal activity indirectly and non-invasively in iNeurons by fluorescence microscopy. Two to three weeks following dox addition, iNeurons displayed a low level of spontaneous activity that was significantly increased with bath application of the neurotransmitter glutamate or the potassium channel blocker tetraethylammonium (TEA; Figure 1D-F). Conversely, activity was inhibited by application of the sodium channel blocker tetrodotoxin (TTX). Though glutamate dramatically increased neuronal activity, it proved to be toxic even at low doses (data not shown). In comparison, iNeurons treated with TEA showed a smaller, sustained increase in activity without significant cell death (Figure 1G). Thus, TEA was utilized in future studies.

bioRxiv preprint doi: https://doi.org/10.1101/648477; this version posted May 24, 2019. The copyright holder for this preprint (which was not certified by peer review) is the author/funder. All rights reserved. No reuse allowed without permission.

To explore a potential connection between hyperexcitability and TDP43 pathology, we pharmacologically stimulated or blocked activity in iNeuron cultures and then examined changes in TDP43 levels via immunocytochemistry (ICC) using an antibody directed against the N-terminus. TEA-treated iNeurons show a significant increase in TDP43 immunoreactivity while TTX-treated iNeurons show a reduction, suggesting a bidirectional relationship between TDP43 abundance and neuronal activity (Figure 1H, I). An analogous relationship was observed via western blot in both iNeurons and rodent primary mixed cortical neurons treated with TEA, TTX, sorbitol, or the GABA receptor antagonist bicuculline (Supplemental Figure 1). However, when we repeated these studies using an antibody directed against the TDP43 C-terminus we failed to identify significant activity-dependent changes in protein abundance (Figure 1J,K).

In addition to a relationship between activity and TDP43 protein levels, these studies revealed striking differences in subcellular TDP43 distribution identified by each antibody. Immunostaining with N-terminal antibodies revealed punctate, cytosolic TDP43 superimposed upon nuclear TDP43. However, only nuclear TDP43 was detected using C-terminal TDP43 antibodies. A survey of commercially available antibodies with known epitopes revealed similar trends in localization: antibodies that recognize the TDP43 N-terminus are more likely to display nuclear and cytosolic staining patterns[49–51], while antibodies specific to the C-terminus primarily show nuclear TDP43[52,53].

Given the variability in antibody specificity and potential difficulties in reproducing results using different antibodies[54,55], we validated our findings by fluorescently-labeling native TDP43 in iPSCs using CRISPR/Cas9 genome engineering. To minimize off-target effects, we used a dual-nickase approach[56] to fuse the green-fluorescent protein Dendra2 to either the N-terminus (D2-TDP43) or the C-terminus (TDP43-D2) of endogenous TDP43 in human iPSCs (Figure 2A). D2-TDP43 and TDP43-D2 iPSCs were differentiated into iNeurons as described before (Figure 2B, C), and neuronal activity was pharmacologically stimulated or blocked using TEA or TTX, respectively. After 48h, we visualized native Dendra2-labeled TDP43 by fluorescence

bioRxiv preprint doi: https://doi.org/10.1101/648477; this version posted May 24, 2019. The copyright holder for this preprint (which was not certified by peer review) is the author/funder. All rights reserved. No reuse allowed without permission.

microscopy, noting a bidirectional relationship between D2-TDP43 abundance and neuronal activity (Figure 2D) that was nearly identical to what we observed using anti-TDP43 antibodies that recognize the N-terminus (Figure 1H, I). In comparison, there were no significant activity-dependent changes in TDP43-D2 (Figure 2E), consistent with our inability to detect changes upon staining with antibodies raised against the TDP43 C-terminus (Figure 1J, K). These data provide convincing evidence for TDP43 species harboring the N- but not the C-terminus that are regulated by neuronal activity. Additionally, the distinctive TDP43 distribution patterns revealed by N- and C-terminal reactive antibodies were reflected by the localization of Dendra2-tagged native TDP43: D2-TDP43 appeared both cytosolic and nuclear (Figure 2B), while the distribution of TDP43-D2 was limited to the nucleus (Figure 2C).

Collectively, these results suggest that neuronal activity elicits an increase in cytosolic TDP43 that lacks a C-terminus. In contrast to what we observed with N-terminal TDP43, there was no reciprocal activity-dependent change in C-terminal TDP43 abundance or localization by immunocytochemistry, and we failed to observe any differences in C-terminally labeled TDP43-D2 upon addition of TEA or TTX, arguing against a cleavage event. Previous studies demonstrated that neuronal activity regulates the abundance of similar RNA-binding proteins through alternative splicing[57,58]. We therefore considered the possibility that activity gives rise to distinct TDP43 isoforms through alternative splicing.

Hyperexcitability drives *TARDBP* alternative splicing

Using available RNA-seq data obtained from human cell lines[59], we identified two alternatively spliced *TARDBP* isoforms predicted to encode C-terminally truncated or shortened (s) TDP43 isoforms (Figure 3A). Identical sTDP43 splice isoforms (TDP-S6 and TDP-S7) were detected in previous studies of *TARDBP* splicing[60,61]. Both sTDP43-specific splice donors are located within *TARDBP* exon 6 and differ by only 9 bp; each utilizes an identical splice acceptor

bioRxiv preprint doi: https://doi.org/10.1101/648477; this version posted May 24, 2019. The copyright holder for this preprint (which was not certified by peer review) is the author/funder. All rights reserved. No reuse allowed without permission.

within the *TARDBP* 3' untranslated region (UTR), thereby eliminating the majority of exon 6 (Figure 3B). We designed primers specific for both sTDP43 splice junctions as well as full-length (fl) TDP43 utilizing the canonical termination codon within exon 6, and utilized qRT-PCR to examine changes in splice isoform abundance in vehicle- or TEA-treated human iNeurons. Both sTDP43 isoforms were not only detectable in iNeurons, but also significantly upregulated by treatment with TEA (Figure 3C), suggesting that the increase in N-terminal TDP43 observed in TEA-treated iNeurons may be due to elevated expression of sTDP43 transcript isoforms. Additionally, however, and in contrast to what we observed for flTDP43 protein (Figures 1,2), transcripts encoding flTDP43 were also upregulated by TEA. Thus, although all *TARDBP* transcript variants increase with neuronal activity, only sTDP43 isoforms demonstrate an analogous increase at the protein level, perhaps due to selective translation of sTDP43 isoforms or nuclear retention of spliced full-length transcripts[61–63].

The two sTDP43 transcripts (sTDP43-1 and -2) encode proteins that differ by only 3 amino acids, and both lack residues that correspond to the entirety of the glycine rich domain (residues 281-414 of flTDP43)[64]. Usage of the common splice acceptor for sTDP43-1 and -2 located within the *TARDBP* 3'UTR results in the inclusion of a new exon encoding a unique 18-amino acid C-terminus not found in flTDP43 (Figure 3D). These splicing events and the novel C-terminus are highly conserved at both the transcript (Supplemental Table 1) and protein (Supplemental Table 2) levels in humans, non-human primates, and lesser mammals. Despite this, and the previous identification of sTDP43 splice variants in human and murine tissues[60,61,64,65], their regulation remained unknown and unexplored. Our results demonstrate that sTDP43 variants are dynamically and bi-directionally regulated by neuronal activity, with neuronal hyperactivity resulting in a significant 2-fold upregulation of sTDP43 at the RNA and protein levels.

bioRxiv preprint doi: https://doi.org/10.1101/648477; this version posted May 24, 2019. The copyright holder for this preprint (which was not certified by peer review) is the author/funder. All rights reserved. No reuse allowed without permission.

sTDP43 is cytosolically localized due to a putative NES in its C-terminal tail

To investigate sTDP43 localization, we transfected rodent primary mixed cortical neurons with diffusely localized mApple to enable visualization of neuronal cell bodies and processes, as well as constructs encoding flTDP43 or sTDP43-1 isoforms fused to an EGFP tag. We then imaged cultures by fluorescence microscopy to examine the localization of each isoform. As expected, flTDP43 appeared to be primarily nuclear in distribution, but sTDP43 demonstrated prominent cytosolic deposition (Figure 4A). The dramatic difference in sTDP43 localization was unanticipated given the presence of an intact nuclear localization signal (NLS) within the sTDP43 N-terminus (Figure 3D), and hinted at the presence a potential nuclear export signal (NES) within the novel sTDP43 C-terminus.

To explore this possibility, we utilized NetNES1.1, an algorithm that employs neural networks and hidden Markov models to predict NES-like motifs from protein primary structure[66]. This analysis uncovered a series of amino acids near the sTDP43 C-terminal pole that could potentially act as an NES (Figure 4B). We then tested the function of this putative NES through two complementary experiments. First, we altered the putative NES within sTDP43 by site-directed mutagenesis (TSLKV→GGGGG) and expressed this construct (sTDP43(mNES)) in rodent primary neurons (Figure 4A). Protein localization was assessed by automated microscopy, using scripts that measure fluorescence separately within cytosolic and nuclear regions of interest (ROIs) and calculate a nuclear-cytoplasmic ratio (NCR) for TDP43 in each transfected neuron[14,15]. While sTDP43 was largely cytosolic (NCR=6.1), sTDP43(mNES) displayed a primarily nuclear localization (NCR=13.8), more so even than flTDP43 (NCR=9.4), suggesting that the putative

bioRxiv preprint doi: https://doi.org/10.1101/648477; this version posted May 24, 2019. The copyright holder for this preprint (which was not certified by peer review) is the author/funder. All rights reserved. No reuse allowed without permission.

NES is necessary for cytosolic deposition of sTDP43 (Figure 4C). Second, we fused EGFP to the 18-amino acid tail of sTDP43 (EGFP-tail), or a version of the sTDP43 tail harboring a mutated NES (EGFP-tail(mNES)) (Figure 4D). For comparison, we also expressed Shuttle-RFP, a construct with a strong NES and a weak NLS that exhibits a predominant cytosolic distribution (NCR=1.3)[67]. Attaching the sTDP43 tail was sufficient to partially exclude EGFP-tail from the nucleus (NCR=2.6) compared to EGFP alone (NCR=3.3), but this change in distribution was eliminated by mutating the residues making up the putative NES in EGFP-tail(mNES) (NCR=3.2) (Figure 4E). Together, these data suggest that the novel C-terminus of sTDP43 encodes a functional NES that facilitates the cytosolic accumulation of sTDP43.

sTDP43 overexpression is highly toxic to neurons

TDP43 mislocalization is a widely observed phenomenon in ALS, and cytosolic TDP43 is a strong predictor of cell death[14]. Given these data and the largely cytosolic localization of sTDP43, we surmised that sTDP43 accumulation would be toxic to mammalian neurons. We therefore utilized automated microscopy in conjunction with survival analysis to track individual neurons prospectively over time and determine their risk of death in an unbiased and high-throughput manner[14,15,59,68,69]. Rodent primary mixed cortical neurons were transfected with mApple and EGFP-tagged TDP43 isoforms and imaged by fluorescence microscopy at 24h intervals for 10d[70]. Custom scripts were used to automatically generate ROIs corresponding to each cell and determine time of death based on rounding of the soma, retraction of neurites, or loss of fluorescence (Figure 5A). The time of death for individual neurons was used to calculate the risk of death in each population relative to a reference group, in this case neurons expressing EGFP[70,71]. In keeping with the results of previous studies, flTDP43 overexpression resulted in a significant increase in the risk of death in comparison to EGFP alone (HR=2.22 $p<2x10^{-16}$). sTDP43-1 overexpression elicited a similar increase in the risk of death for transfected neurons

bioRxiv preprint doi: https://doi.org/10.1101/648477; this version posted May 24, 2019. The copyright holder for this preprint (which was not certified by peer review) is the author/funder. All rights reserved. No reuse allowed without permission.

(HR=1.90 $p<2x10^{-16}$), suggesting that sTDP43 and flTDP43 display similar toxicities when overexpressed in neurons (Figure 5B).

sTDP43 alters endogenous TDP43 localization

TDP43 dimerizes via its N-terminus[52,72–78], and because sTDP43 is exported from the nucleus and contains an intact N-terminus we questioned whether sTDP43 might bind to and sequester endogenous TDP43 within the cytosol. To determine if sTDP43 is capable of dimerizing with endogenous TDP43, we transfected HEK293T cells with HaloTag-labeled sTDP43-1 or flTDP43 and isolated the fusion proteins using HaloLink resin (Figure 6A). We detected equivalent amounts of endogenous TDP43 in eluates from sTDP43-HaloTag and flTDP43-HaloTag, indicating that sTDP43 effectively binds endogenous TDP43 (Figure 6B). We also examined the interaction between sTDP43 and endogenous TDP43 by ICC. HEK293T cells were transfected with EGFP or EGFP-tagged sTDP43, immunostained using a C-terminal TDP43 antibody that recognizes endogenous TDP43 but not sTDP43, and imaged by confocal fluorescence microscopy (Figure 6C). HEK293T cells overexpressing EGFP-tagged sTDP43 displayed cytosolic inclusions that strongly colocalize with endogenous TDP43. Moreover, we observed significant reductions in nuclear endogenous TDP43 in association with cytosolic TDP43 deposition (Figure 6D,E), suggesting cytosolic sequestration of endogenous TDP43 by sTDP43. Rodent primary mixed cortical neurons overexpressing sTDP43-1 displayed a similar depletion of endogenous TDP43 from the nucleus (Figure 6F,G). We did not observe significant increases in cytosolic TDP43 deposition in transfected neurons (Figure 6H), potentially due to TDP43 aggregation and subsequent masking of the antibody epitope, as previously noted[61]. Thus, sTDP43 overexpression results in both cytoplasmic deposition and nuclear clearance of endogenous TDP43, recapitulating signature features of ALS pathology and implicating that both gain- and loss-of-function mechanisms contribute to toxicity.

bioRxiv preprint doi: https://doi.org/10.1101/648477; this version posted May 24, 2019. The copyright holder for this preprint (which was not certified by peer review) is the author/funder. All rights reserved. No reuse allowed without permission.

sTDP43 lacks canonical functions of flTDP43

To further examine the possibility that sTDP43 elicits loss-of-function toxicity, we assessed the ability of sTDP43 to participate in TDP43-related splicing activity. In keeping with TDP43's function as a splicing repressor, TDP43 effectively blocks the inclusion of cystic fibrosis transmembrane conductance regulator (CFTR) exon 9 (Supplemental Figure 2A)[79,80]. In HEK293T cells expressing a CFTR minigene reporter, cotransfection with EGFP-flTDP43 resulted in proficient exon 9 exclusion as measured by PCR. In contrast, EGFP-sTDP43-1 expression failed to significantly affect exon 9 exclusion (Supplemental Figure 2B,C), suggesting that without the C-terminus, sTDP43 is incapable of TDP43-specific splicing[60,64,65].

Functional flTDP43 also participates in an autoregulatory feedback loop, in which flTDP43 recognizes sequences within the *TARDBP* 3'UTR, triggering alternative splicing and/or polyadenylation and subsequent mRNA degradation[81,82]. To determine if sTDP43 is able to regulate endogenous TDP43 expression via this mechanism, we employed a TDP43 autoregulation reporter consisting of an open reading frame (ORF) encoding the fluorescent protein mCherry upstream of the *TARDBP* 3' UTR (Supplemental Figure 3A)[68]. In rodent primary cortical neurons expressing the TDP43 autoregulation reporter, cotransfection with EGFP-tagged flTDP43 resulted in a decrease in reporter signal, as expected. EGFP-labeled sTDP43-1 displayed more subtle effects on reporter fluorescence, suggesting that its ability to autoregulate TDP43 is impaired (Supplemental Figure 3B,C). Together, these results indicate that sTDP43 lacks many of the canonical functions of TDP43, including its splicing and autoregulatory abilities.

sTDP43 colocalizes with stress granule markers

Previous studies suggested that sTDP43 associates with protein components of cytoplasmic stress granules, including G3BP1 and TIA1[65]. Therefore, we immunostained for

bioRxiv preprint doi: https://doi.org/10.1101/648477; this version posted May 24, 2019. The copyright holder for this preprint (which was not certified by peer review) is the author/funder. All rights reserved. No reuse allowed without permission.

G3BP1 and TIA1 in HEK293T cells overexpressing EGFP-tagged sTDP43-1, before and after application of osmotic stress (0.4M sorbitol). Prior to sorbitol treatment, we noted substantial colocalization of sTDP43-1 with G3BP1 (Supplemental Figure 4A) and TIA1 (data not shown) in large cytoplasmic deposits; these structures were unique to cells transfected with sTDP43-1, suggesting that sTDP43 overexpression elicits the formation of irregular structures rich in stress granule components. However, when cells were stressed with 0.4M sorbitol we observed the formation of multiple small, punctate granules that colocalize with both G3BP1 and TIA1, as well as endogenous TDP43 (Supplemental Figure 4B). These data confirm that sTDP43 localizes to stress granules, and further imply that sTDP43 production may be sufficient for the assembly of cytoplasmic stress granule-like structures even in the absence of stress.

sTDP43 transcripts are enriched in murine and human lumbar motor neurons

To determine if sTDP43 isoforms are produced *in vivo* and assess their expression in different regions of the central nervous system, we took advantage of a previous study that analyzed the transcriptome from murine frontal cortex and lumbar spinal motor neurons isolated by laser capture microdissection (Figure 7A)[83]. The most abundant splice isoform detected in frontal cortex homogenate was flTDP43, with predominant use of the conventional termination codon within *TARDBP* exon 6. However, splicing of the *TARDBP* locus, and in particular exon 6 and the 3'UTR, was dramatically altered in murine spinal motor neurons. In contrast to what was observed in frontal cortex, two splicing events corresponding to sTDP43 variants 1 and 2 were strongly favored in spinal motor neurons—these isoforms were upregulated ~12- and 10-fold, respectively, in lumbar spinal neurons relative to frontal cortex (Figure 7B,C). Moreover, the predicted amino acid sequences for these splice isoforms were identical to those of sTDP43-1 and sTDP43-2, including the shared 18-amino acid C-terminus (Figure 7A). These data show that

bioRxiv preprint doi: https://doi.org/10.1101/648477; this version posted May 24, 2019. The copyright holder for this preprint (which was not certified by peer review) is the author/funder. All rights reserved. No reuse allowed without permission.

sTDP43 isoforms are not only detectable *in vivo* within the murine CNS, but they are also significantly upregulated in spinal motor neurons, a cell type selectively targeted in ALS.

We also examined sTDP43 expression in human spinal neurons utilizing published RNA-seq data on laser-captured lumbar spinal motor neurons, isolated from control and sporadic (s) ALS patient tissue[84]. Within this dataset, we identified specific transcripts corresponding to flTDP43, sTDP43-1, and sTDP43-2 based on sequence, and characterized the remaining *TARDBP* variants as "other." Although there was no apparent difference in the abundance of any *TARDBP* transcripts between sALS and control motor neurons, we noted a dramatic enrichment of sTDP43-1 transcripts in spinal neurons, in comparison to flTDP43, sTDP43-2, and other *TARDBP* variants (Figure 7D,E). We also examined available RNA-seq data on spinal cord ventral horn homogenate derived from control and sALS patients[85], as well as cerebellum and frontal cortex derived from controls, sALS, and patients bearing disease-associated mutations in *C9orf72* (C9ALS)[86]. Fundamental differences in sample preparation and sequencing methodology among each study (Supplemental Figure 5A) prevents the direct comparison of sTDP43 abundance between tissue types. Despite these limitations, it is clear sTDP43-1 but not sTDP43-2 is expressed in several different regions of the CNS, including but not limited to spinal motor neurons, frontal cortex, and cerebellum, though it is not significantly upregulated in sALS or C9ALS (Supplemental Figure 5B,C).

Endogenously produced sTDP43 is detectable using specific antibodies

To distinguish natively-produced sTDP43 species, we generated an antibody directed against the novel 18-amino acid C-terminus of sTDP43 (Figure 3D). This antibody specifically recognized EGFP fused to the sTDP43 C-terminus, suggesting that the sTDP43 tail is sufficient for immunoreactivity (Figure 8A). Furthermore, the signal was completely abolished by

bioRxiv preprint doi: https://doi.org/10.1101/648477; this version posted May 24, 2019. The copyright holder for this preprint (which was not certified by peer review) is the author/funder. All rights reserved. No reuse allowed without permission.

preincubation with the immunizing peptide, indicating good sequence specificity. We further validated the antibody by transfecting HEK293T cells with EGFP-tagged sTDP43-1, isolating RIPA- and urea-soluble protein fractions, and immunoblotting for sTDP43. Previous studies demonstrated that overexpressed sTDP43 is highly insoluble[64]; supporting this, we detected EGFP-sTDP43 exclusively in the urea-soluble fraction while EGFP-flTDP43 appeared in both RIPA- and urea-soluble fractions (Figure 8B). We also tested the sTDP43 antibody in human iNeurons treated with TEA or TTX to induce or abolish neuronal activity, respectively (Figure 8C). In these studies, sTDP43 immunoreactivity was significantly increased by TEA and reduced by TTX (Figure 8D), consistent with activity-dependent upregulation of N-terminally labeled D2-TDP43 (Figure 2) and its detection by antibodies specific for the TDP43 N-terminus (Figure 1). Notably, sTDP43 antibodies detected numerous cytosolic puncta in TEA-treated neurons that were less apparent in vehicle- and TTX-treated cells, and the background nuclear signal was minimal in all cases. These data indicate that sTDP43 antibodies selectively detect truncated, cytosolic, and insoluble TDP43 species by western blot and ICC, establishing them as useful tools for investigating sTDP43 deposition and its potential role in neurodegeneration.

Based on the observed upregulation of sTDP43 splice isoforms in lumbar spinal neurons, we employed our newly-developed sTDP43 antibody for detecting sTDP43 *in vivo* within murine spinal cord sections. As predicted from the RNA-sequencing data, we detected cytoplasmic sTDP43 in anterior horn neurons from the lumbar spinal cord, confirming the subcellular distribution of the protein originally noted *in vitro* (Supplemental Figure 6A). We also observed strong colocalization of sTDP43 with GFAP-positive astrocytic projections within the spinal white matter, indicating astrocytic expression of sTDP43 (Supplemental Figure 6B). Subsequent studies confirmed that sTDP43 is endogenously produced by human iPSC-derived astrocytes (Supplemental Figure 7), suggesting that while sTDP43 is enriched within spinal neurons (Figure 7), it is also synthesized by supporting glia.

bioRxiv preprint doi: https://doi.org/10.1101/648477; this version posted May 24, 2019. The copyright holder for this preprint (which was not certified by peer review) is the author/funder. All rights reserved. No reuse allowed without permission.

sTDP43 pathology is observed in ALS patient tissue

Given that (a) sTDP43 is endogenously produced at relatively high levels in spinal neurons, (b) neuronal hyperexcitability is a conserved feature of ALS, and (c) sTDP43 is upregulated by neuronal activity, we suspected that sTDP43 may accumulate in individuals with sALS. To address this question, we immunostained human cortex and spinal cord sections from sALS and unaffected control patients using antibodies that recognize the TDP43 N-terminus or our newly-developed sTDP43 antibodies (Figure 8E). Control tissue showed primarily nuclear N-terminal TDP43 and low immunoreactivity for sTDP43 in both the cortex and spinal cord. As predicted for patients with sALS, immunostaining with N-terminal TDP43 antibodies showed both a reduction in nuclear signal and the appearance of cytoplasmic inclusions in ALS patient tissue. Notably, and in contrast to what is observed in control tissues, sTDP43 immunoreactivity was markedly elevated in both spinal cord and cortex from sALS patients. sTDP43-positive inclusions closely colocalized with the cytoplasmic inclusions but not the residual nuclear TDP43 detected by N-terminal TDP43 antibodies, suggesting that sTDP43 antibodies specifically label cytosolic deposits in sALS tissue.

In light of endogenous sTDP43 detected within mouse spinal cord astrocytes (Supplemental Figure 6B) and human iPSC-derived astrocytes (Supplemental Figure 7), we asked if sTDP43 pathology might also be present within astrocytes. In sections from controls and sALS patients immunostained with sTDP43 antibodies, neurons and glia were identified by co-staining with NeuN and GFAP antibodies, respectively (Figure 8F). Cytoplasmic sTDP43 accumulations were detected in both NeuN-positive neurons and GFAP-positive astrocytes, suggesting that sTDP43 pathology is not limited to neurons. Taken together, these results demonstrate that endogenous sTDP43 accumulates within neurons and glia of individuals with ALS, supporting a potentially pathogenic contribution of sTDP43 isoforms to ALS pathogenesis.

bioRxiv preprint doi: https://doi.org/10.1101/648477; this version posted May 24, 2019. The copyright holder for this preprint (which was not certified by peer review) is the author/funder. All rights reserved. No reuse allowed without permission.

Discussion

In this study, we show that neuronal hyperactivity leads to the selective upregulation of C-terminally truncated TDP43 isoforms (sTDP43). These isoforms are intrinsically insoluble and accumulate within cytoplasmic aggregates by virtue of a NES present within a novel 18-amino acid C-terminus. sTDP43 also sequesters endogenous TDP43 within cytoplasmic aggregates and induces its clearance from the nucleus, thereby recapitulating signature pathologic changes found in the majority of individuals with ALS and implicating complementary gain- and loss-of-function mechanisms in disease pathogenesis. sTDP43 transcripts are enriched in murine motor neurons, a cell type that is selectively vulnerable in ALS, and post-mortem samples from individuals with ALS show a striking accumulation of sTDP43 within affected neurons and glia. These observations suggest a fundamental link between neuronal hyperexcitability and TDP43 pathology, two conserved features characteristic of both familial and sporadic ALS. Moreover, they raise the possibility that sTDP43 production and/or its accumulation are heretofore-unrecognized contributors to neurodegeneration in ALS.

A series of previous studies demonstrated that alternative splicing of *TARDBP* gives rise to truncated TDP43 isoforms lacking the C-terminus that are highly insoluble when overexpressed in heterologous systems[49,60,64]. Here, we show for the first time that neuronal activity selectively upregulates these truncated isoforms, which we collectively labeled sTDP43, despite an increase in transcripts encoding full-length as well as sTDP43 isoforms. This discrepancy may arise from different 3'UTR splicing patterns for each of the variants, resulting in nuclear retention and/or destabilization of mRNAs encoding flTDP43 but not sTDP43[61–63,81,82]. As such, the activity-dependent and apparently selective upregulation of sTDP43, together with the widespread neuronal hyperactivity observed in ALS patients, animal models, and human iPSC-derived neurons[26,28,34,35,42,43], may be a crucial factor driving sTDP43 deposition in ALS tissue.

bioRxiv preprint doi: https://doi.org/10.1101/648477; this version posted May 24, 2019. The copyright holder for this preprint (which was not certified by peer review) is the author/funder. All rights reserved. No reuse allowed without permission.

In keeping with previous studies[65], overexpressed sTDP43 accumulates in the cytoplasm where it often forms large, insoluble inclusions. The low-complexity domain (LCD) within the TDP43 C-terminus is essential for liquid-phase separation[87–90], and has been heavily implicated in TDP43 aggregation. Even so, our observations and those of others[64,65] show that sTDP43 is insoluble and prone to aggregation, despite lacking the LCD. A growing body of evidence suggests that proteins with complex, folded domains such as the TDP43 RNA recognition motifs (RRMs) are highly susceptible to aggregation[91]. Rather than promoting insolubility, the presence of LCDs within these proteins protects against misfolding and aggregation by enabling reversible phase transitions during conditions of supersaturation. Thus, LCDs may permit higher local concentrations of RRM-containing proteins than would otherwise be possible without misfolding and/or aggregation[92]. In this regard, the absence of the LCD may be directly responsible for the enhanced aggregation of sTDP43; indeed, several RNA-binding proteins display similar phenotypes upon removal of the LCD, including Pub1, Pab1 and Sup35[92–95].

Using predictive software, we identified a potential NES located within the novel 18-amino acid sTDP43 tail, and experimentally confirmed that this segment is necessary and sufficient for sTDP43 cytoplasmic localization. Thus, despite the presence of a functional NLS within sTDP43, the NES appears to be dominant, either due to a high affinity for nuclear exporters or because of enhanced accessibility of the NES at the extreme C-terminus of the protein.

sTDP43 lacks the C-terminal glycine rich domain required for splicing activity[96]; as such, sTDP43 is incapable of *CFTR* minigene splicing or effectively participating in TDP43 autoregulation, which involves differential splicing of the *TARDBP* 3'UTR[81,82]. The C-terminal glycine rich domain is also required for toxicity upon TDP43 overexpression in yeast[97]. Despite this, sTDP43 overexpression was still lethal in neurons. We suspect that sTDP43-related toxicity arises from a combination of factors, including (a) the NES within the new C-terminal tail region provoking cytoplasmic sTDP43 deposition; (b) its interaction with endogenous flTDP43 via its N-

bioRxiv preprint doi: https://doi.org/10.1101/648477; this version posted May 24, 2019. The copyright holder for this preprint (which was not certified by peer review) is the author/funder. All rights reserved. No reuse allowed without permission.

terminus[52,72,98]; and (c) the presence of intact RNA-recognition motifs that enable sTDP43 to bind and potentially sequester cytoplasmic mRNAs.

sTDP43 isoforms are highly conserved in humans, non-human primates, and lesser mammals at the transcript and protein levels. Such evolutionary conservation suggests that these isoforms fulfill unknown functions, perhaps involving a compensatory response to chronic neuronal hyperactivity or generalized stress. Intriguingly, sTDP43 transcripts are significantly enriched in murine motor neurons compared to frontal cortex homogenate, and sTDP43-1 is the dominant *TARDBP* species in human lumbar motor neurons, raising the possibility that spinal motor neurons accumulate potentially toxic levels of sTDP43 in the setting of hyperexcitability. Future studies are needed to determine whether native sTDP43 performs an essential function in motor neurons or other cell types, and if sTDP43 contributes to the selective vulnerability of motor neurons in ALS[99,100].

By creating a unique antibody that recognizes the novel C-terminus of sTDP43, we detected cytoplasmic sTDP43 inclusions selectively within the spinal cord and cortex of ALS patients. In addition, the presence of sTDP43 deposits coincided with nuclear TDP43 exclusion, as predicted by sTDP43 nuclear export and its affinity for flTDP43. Although the aggregation-prone[101] TDP43 C-terminus forms a core component of the cytoplasmic inclusions found in ALS patients[102–109], emerging evidence suggests that N-terminal TDP43 fragments also contribute to ALS pathogenesis. N-terminal TDP43 fragments are observed in ALS patient spinal cord[110,111], and in keeping with studies of RNA-binding proteins in yeast, the TDP43 RRMs misfold and aggregate in vitro without the C-terminal LCD to maintain solubility[65,91,93–95,112–114]. Independent of the RRMs, the TDP43 N-terminus enhances TDP43 aggregation and toxicity[65,78,112,113], potentially adding to sTDP43 insolubility and the impact of sTDP43 deposition in affected neurons.

TDP43-positive cytoplasmic inclusions in ALS are not limited to neurons but are also found in astrocytes and oligodendrocytes[115–118]. Astrocytes help regulate extracellular glutamate levels, and their dysfunction in ALS may lead to impaired synaptic glutamate buffering in sporadic as

bioRxiv preprint doi: https://doi.org/10.1101/648477; this version posted May 24, 2019. The copyright holder for this preprint (which was not certified by peer review) is the author/funder. All rights reserved. No reuse allowed without permission.

well as familial ALS[119–124]. In addition to detecting endogenous sTDP43 production in cultured human astrocytes and murine spinal cord, we noted disease-specific astrocyte sTDP43 pathology in sALS patient tissue. Although the effect of sTDP43 accumulation in these cells remains to be determined, it is possible that sTDP43-induced astrocyte toxicity triggers a feed-forward mechanism in which reduced glutamate buffering results in neuronal hyperactivity, increased sTDP43 production, and subsequent neurodegeneration.

Our work underlines the significance of previously identified TDP43 isoforms and highlights a pivotal connection between neuronal hyperexcitability and TDP43 pathology, two conserved findings in ALS. Many questions remain, including the function of sTDP43 isoforms and whether cell type-specific differences in sTDP43 expression or metabolism contribute to the selective vulnerability of motor neurons in ALS. Additional investigations of sTDP43 splicing and its regulation are needed to determine if targeted manipulation of sTDP43 production has the potential to prevent or slow motor neuron degeneration in ALS.

Materials and Methods

Generation and maintenance of iPSCs

Fibroblasts were reprogrammed into iPSCs via transfection with episomal vectors encoding seven reprogramming factors[125] and validated as previously described[126]. All iPSC lines were cultured in Essential 8 (E8) media (Gibco A1517001) on plates coated with vitronectin (Gibco A14700) diluted 1:100 in Mg^{2+}/Ca^{2+}-free phosphate buffered saline (PBS, Gibco 14190-144). Cells were passaged every 5–6d using 0.5 mM EDTA (Sigma E7889) dissolved in PBS followed by gentle trituration in E8 media with a P1000 pipette. All lines are verified mycoplasma-free on a monthly basis.

Integration of Ngn1/Ngn2 cassette into iPSCs

bioRxiv preprint doi: https://doi.org/10.1101/648477; this version posted May 24, 2019. The copyright holder for this preprint (which was not certified by peer review) is the author/funder. All rights reserved. No reuse allowed without permission.

iPSCs were split and plated into a vitronectin-coated 6 well plate as described above, at a density such that cells were 50-70% confluent in clumps of 2-5 cells at the time of transfection. Following plating, cells were incubated overnight in E8 media with ROCK inhibitor (Fisher BDB562822), and changed into fresh E8 media the following morning. Thirty minutes prior to transfection (~24h after plating or when the density was 50-70%), cells were changed into mTESR-1 media (Cell Technologies 85850) and then transfected with 2.5 µg of donor DNA and 1.25 µg of each targeting construct (Supplemental Table 3) using Lipofectamine Stem (Invitrogen STEM00003) according to the manufacturer's instructions. The following morning, cells were changed into fresh E8 media. Media was changed daily, and cells were screened for red fluorescence. When the partially positive colonies reached 100-500 cells, they were carefully scraped/aspirated using a P200 pipet tip and transferred to a new vitronectin-coated dish. This process was repeated, enriching the fluorescent cells until a 100% fluorescent colony was identified. This was then relocated to a new dish, and expanded for future use. The Ngn1/2 integration cassette and accompanying targeting constructs were a gift from M. Ward.

iNeuron differentiation

Day 0. Induced pluripotent stem cells were washed in PBS and incubated in prewarmed accutase (Sigma A6964) at 37°C for 8m. Four volumes of E8 media were added to the plate, and the cells were collected and pelleted at 200xg for 5m. The media was aspirated, and the pellet was resuspended in 1ml of fresh E8 media. Cells were counted using a hemocytometer, diluted, plated at a density of 20,000 cells/ml in E8 media with ROCK inhibitor and incubated at 37°C overnight. **Day 1.** Media was changed to N2 media (1x N2 Supplement (Gibco 17502-048), 1x NEAA Supplement (Gibco 11140-050), 10 ng/ml BDNF (Peprotech 450-02), 10 ng/ml NT3 (Peprotech 450-03), 0.2 µg/ml laminin (Sigma L2020), 2 mg/ml doxycycline (Sigma D3447) in E8 media). **Day 2.** Media was changed to transition media ((1x N2 Supplement, 1x NEAA Supplement, 10 ng/ml BDNF, 10 ng/ml NT3, 0.2 µg/ml laminin, 2 mg/ml doxycycline in half E8 media, half DMEM F12

bioRxiv preprint doi: https://doi.org/10.1101/648477; this version posted May 24, 2019. The copyright holder for this preprint (which was not certified by peer review) is the author/funder. All rights reserved. No reuse allowed without permission.

(Gibco 11320-033)). **Day 3.** Media was changed into B27 media (1x B27 Supplement (Gibco 17504-044), 1x Glutamax Supplement (Gibco 35050-061), 10 ng/ml BDNF, 10 ng/ml NT3, 0.2 µg/ml laminin, 2 mg/ml doxycycline, and 1x Culture One (Gibco A33202-01) in Neurobasal-A (Gibco 12349-015)). **Day 6.** An equal volume of B27 media without Culture One was added to each well. **Day 9-21.** All cultures underwent a half-media change every 3d in fresh B27 media.

Immunocytochemistry

Neurons were fixed with 4% paraformaldehyde (PFA; Sigma P6148), rinsed with PBS, and permeabilized with 0.1% Triton X-100 (Bio-rad 161-0407) in PBS. Neurons were then treated with 10 mM glycine (Fisher BP381-1) in PBS, and incubated in a blocking solution (0.1% Triton X-100, 2% fetal calf serum (Sigma F4135), and 3% bovine serum albumin (BSA, Fisher BP9703-100) in PBS) at room temperature for 1h before incubation overnight at 4°C in primary antibody diluted in blocking buffer (Supplemental Table 4). Cells were then washed 3x in PBS and incubated at room temperature with Alexa Fluor 488 goat anti-rabbit (Life Technologies A11034), Alexa Fluor goat anti-mouse 594 (Life Technologies A11032), or Alexa Fluor donkey anti-rabbit 647 (Life Technologies A31573) secondary antibody diluted 1:5000 in blocking solution for 1h. Following 3x washes in PBS containing 1:10000 Hoechst 33258 dye (Invitrogen H3569), neurons were imaged via fluorescence microscopy. High resolution images were obtained on a Zeiss LSM 800 with a 63x NA1.4 Oil/DIS Plan-Apochromat objective. Excitation was accomplished using 405, 488, 561, and 633 nm lasers.

Modulation of neuronal activity

Half of the existing media was removed from rat cortical neurons or mature human iNeurons and replaced with fresh media and drug such that the final concentration on the cells was 4 mM tetraethylammonium chloride (TEA, Sigma T2265)**,** 2 µM tetrodotoxin citrate (TTX, R&D Systems

bioRxiv preprint doi: https://doi.org/10.1101/648477; this version posted May 24, 2019. The copyright holder for this preprint (which was not certified by peer review) is the author/funder. All rights reserved. No reuse allowed without permission.

1078) or 25 mM glutamate (Sigma G1251) alongside a volume-matched vehicle control. Cells were incubated at 37° C for 48h, then fixed, imaged, or harvested as needed.

Monitoring calcium transients

Mature iNeurons—differentiated as previously described from an iPSC line stably expressing gCaMP6f and mCherry[48]—were imaged for 100ms at 200ms intervals for a total of 100 frames, for a cumulative a 20s observation window. One location was imaged per well for 2-30 instances over a 6-12h period. Each neuron was identified as a region of interest using mCherry fluorescence, and the intensity of gCaMP6f signal was plotted over time. Individual traces were corrected for photobleaching, normalized to the median of each imaging period, and filtered for peaks below a discrete threshold to aid in spike identification. The number of peaks for each neuron and each imaging period was manually counted using a custom-designed graphical user interface. Events per second were averaged for each cell and compared across groups.

CRISPR/Cas9 editing of iPSCs

Oligos complementary to the target region (Supplemental Table 3) were annealed, digested, and ligated into the *BbsI* site in pX335-U6-Chimeric_BB-CBh-hSpCas9n(D10A) (Addgene #42335, deposited by Feng Zhang) or pX330S-4 (Addgene #58780, deposited by Feng Zhang) according to the protocol available from Addgene. iPSCs stably expressing Ngn1-2 under a dox-inducible promoter were split and transfected as described above with pX335 vectors encoding Cas9(D10A) and sgRNA pairs targeting sequences flanking the *TARDBP* start codon for D2-TDP43 or stop codon for TDP43-D2. Cells were cotransfected with the appropriate HDR vector encoding the Dendra2 open reading frame flanked by 400 bp of sequence homologous to that surrounding the *TARDBP* start codon (D2-TDP43) or stop codon (TDP43-D2) (in pUC-minus(M), synthesized by Blue Heron, LLC). Fluorescent cells were selected and successively passaged as

bioRxiv preprint doi: https://doi.org/10.1101/648477; this version posted May 24, 2019. The copyright holder for this preprint (which was not certified by peer review) is the author/funder. All rights reserved. No reuse allowed without permission.

described above to generate iPSC colonies in which 100% of cells expressed Dendra2-labeled TDP43.

Longitudinal fluorescence microscopy and automated image analysis

Neurons were imaged as described previously[68,69] using a Nikon Eclipse Ti inverted microscope with PerfectFocus3a 20X objective lens and either an Andor iXon3 897 EMCCD camera or Andor Zyla4.2 (+) sCMOS camera. A Lambda XL Xenon lamp (Sutter) with 5 mm liquid light guide (Sutter) was used to illuminate samples, and custom scripts written in Beanshell for use in µManager controlled all stage movements, shutters, and filters. Custom ImageJ/Fiji macros and Python scripts were used to identify neurons and draw both cellular and nuclear regions of interest (ROIs) based upon size, morphology, and fluorescence intensity. Fluorescence intensity of labeled proteins was used to determine protein localization or abundance. Custom Python scripts were used to track ROIs over time, and cell death marked a set of criteria that include rounding of the soma, loss of fluorescence and degeneration of neuritic processes[70].

RNA sequencing

Raw reads from murine frontal cortex and spinal cord[59,83,84], as well as human spinal cord, frontal cortex and cerebellum[59,83,84], were downloaded from Gene Expression Omnibus (GEO) with the SRA Toolkit v2.9.2. Reads were trimmed with TrimGalore v0.6.0 using automatic adapter detection and a minimum Phred score of 20. For alignment-free transcript-level quantification, trimmed reads were quantified using Salmon v0.13.1 (Patro 2017) and imported into the RStudio using txImport v1.12.0 (Soneson 2015) to generate transcript-level summaries[127,128]. The Ensembl genome assemblies and transcript annotations from GRCh38.96 and GRcm38.96 were used as human and mouse references, respectively. For alignment-based analysis of mouse datasets, trimmed reads were aligned with hisat2 v2.0.5 and raw counts were quantified for

bioRxiv preprint doi: https://doi.org/10.1101/648477; this version posted May 24, 2019. The copyright holder for this preprint (which was not certified by peer review) is the author/funder. All rights reserved. No reuse allowed without permission.

unique splice donor/acceptor combinations present in unique *TARDBP* isoforms. In each case, splicing events were visualized using IG Viewer software (Broad Institute).

qRT-PCR

RNA was isolated using the RNeasy Mini Kit (Qiagen 74106), and cDNA was reverse transcribed from 1 ug of the resultant RNA with the Bio-Rad iScript kit (Bio-Rad 170-8891) in a reaction volume of 20 µl. 0.5 µl of cDNA was used for each reaction as a template for quantitative (q)PCR, which was performed using Power SYBR Green (Applied Biosystems A25742) using the primers listed in Supplemental Table 5.

Plasmids

Plasmids pGW1-EGFP(1)[129], pGW1-TDP43-EGFP[130], and pGW1-mApple[130] were used both as experimental controls and to generate additional constructs (Supplemental Table 6).

To generate pGW1-sTDP43-EGFP, a geneblock comprised of the sTPD43-1 open reading frame (ORF) flanked by ApaI and AgeI restriction enzyme sites was generated by Integrated DNA Technologies (IDT). This geneblock was digested with ApaI and AgeI and cloned into the corresponding sites immediately upstream of the EGFP ORF in pGW1-EGFP(1).

To create pGW1-sTDP43(mNES)-EGFP, the sTDP43 open reading frame was amplified using a reverse primer to mutate the putative NES into five sequential glycine resides. The resulting amplicon was digested with ApaI and AgeI and cloned into corresponding sites in pGW1-EGFP(1).

bioRxiv preprint doi: https://doi.org/10.1101/648477; this version posted May 24, 2019. The copyright holder for this preprint (which was not certified by peer review) is the author/funder. All rights reserved. No reuse allowed without permission.

To generate pGW1-EGFP(2), the EGFP open reading frame was PCR amplified from pGW1-EGFP(1). The resultant amplicon was digested with HindIII and Kpn1 restriction enzymes and cloned into the corresponding sites in pGW1-CMV.

To generate pGW1-EGFP-tail, sense and antisense oligomers with the sequence of the 18-amino acid tail were generated by IDT, designed such that annealing would result in cohesive ends identical to cut KpnI and NheI restriction enzyme sites. The annealed oligo was cloned into corresponding sites immediately downstream of the EGFP ORF in pGW1-EGFP(2).

To generate pGW1-EGFP-tail(mNES), sense and antisense oligomers with the sequence of the 18-amino acid tail in which the putative NES was replaced by 5 glycine residues were generated by IDT, designed such that annealing would result in cohesive ends identical to cut KpnI and NheI restriction enzyme sites. The annealed oligo was cloned into corresponding sites immediately downstream of the EGFP ORF in pGW1-EGFP(2).

To create pGW1-EGFP-TDP43, the TDP43 ORF was PCR amplified from pGW1-TDP43-EGFP. The resultant amplicon was digested with KpnI and NheI restriction enzymes and cloned into the corresponding sites immediately downstream of the EGFP ORF in pGW1-EGFP(2).

To generate pGW1-EGFP-sTDP43, the sTDP43-1 ORF was PCR amplified from pGW1-sTDP43-EGFP. The resultant amplicon was digested with KpnI and NheI restriction enzymes and cloned into the corresponding sites immediately downstream of the EGFP ORF in pGW1-EGFP(2).

To create pGW1-Halo, the HaloTag ORF was PCR amplified from pFN21A HaloTag PUM2 RBD R6SYE (a gift from A. Goldstrohm). The resultant amplicon was digested with XbaI and SbfI restriction enzymes and cloned into the corresponding sites in pGW1-CMV.

bioRxiv preprint doi: https://doi.org/10.1101/648477; this version posted May 24, 2019. The copyright holder for this preprint (which was not certified by peer review) is the author/funder. All rights reserved. No reuse allowed without permission.

To create pGW1-TDP43-Halo, the TDP43 ORF was PCR amplified from pGW1-TDP43-EGFP. The resultant amplicon was digested with NheI and AgeI and cloned into corresponding sites in pGW1 to make pGW1-TDP43. The HaloTag ORF was then amplified from pFN21A HaloTag PUM2 RBD R6SYE, digested with XbaI and SbfI restriction enzyme sites and cloned into the corresponding sites immediately downstream of the TDP43 ORF in pGW1-TDP43.

To generate pGW1-sTDP43-Halo, the sTDP43-1 ORF was PCR amplified from pGW1-sTDP43-EGFP. The resultant amplicon was digested with AgeI and NheI and cloned into corresponding sites immediately upstream of the HaloTag ORF in pGW1-Halo.

To generate the TDP43 autoregulatory reporter[130], a 3 kb segment extending from *TARDBP* exon 6 to the 3' UTR was amplified from genomic DNA. The resultant amplicon was digested with BsrGI and SfiI and cloned into corresponding sites immediately downstream of the mCherry ORF in pCAGGs-mCherry.

Shuttle-RFP (pcDNA3.1-NLS-mCherry-NES) was purchased from Addgene (#72660, donated by B. Di Ventura and R. Eils). The CFTR minigene reporter was a gift from Y. Ayala, and pCaggs-mCherry and pGW1-CMV were gifts from S. Finkbeiner. The shTARDBP and non-targeting shRNA constructs were purchased from Dharmacon (V3SH11240-224779127, VSC11712).

All constructs were verified by Sanger sequencing, and described in Supplemental Table 6.

Primary neuron cell culture and transfection

Cortices from embryonic day (E)19-20 Long-Evans rat embryos were dissected and disassociated, and primary neurons were plated at a density of $6x10^5$ cells/ml in 96-well plates,

bioRxiv preprint doi: https://doi.org/10.1101/648477; this version posted May 24, 2019. The copyright holder for this preprint (which was not certified by peer review) is the author/funder. All rights reserved. No reuse allowed without permission.

as described previously[131]. At *in vitro* day (DIV) 4, neurons were transfected with 100 ng pGW1-mApple to mark cell bodies and 50-100 ng of an experimental construct using Lipofectamine 2000 (Invitrogen 52887), as previously described[14,70,130]. Following transfection, cells were placed in either Neurobasal Complete Media (Neurobasal (Gibco 21103-049), 1x B27, 1x Glutamax, 100 units/mL Pen Strep (Gibco 15140-122)) or NEUMO photostable medium with SOS (Cell Guidance Systems M07-500) and incubated at 37°C in 5% CO_2.

Culturing and transfecting HEKs

Human embryonic kidney (HEK) 293T cells were cultured in DMEM (GIBCO 11995065), 10% FBS (Gibco ILT10082147), 1x Glutamax, and 100 units/mL Pen Strep at 37°C in 5% CO_2. HEK293T cells are originally female in origin, are easily transfected, and have been transformed with SV40 T-antigen. HEK293T cells were transfected with Lipofectamine 2000 according to the manufacturer's instructions.

Immunoprecipitation using HaloLink

HEK293T cells were transfected with Halo-tagged constructs of interest. Two days after transfection, cells were collected in PBS and pelleted at 21,000xg for 5m. The cells were then resuspended in 100 µl lysis buffer (50 mM Tris-HCl, 150 mM NaCl, 1% Triton X-100, 0.1% sodium deoxycholate). After incubation on ice for 15m, cells were passed through a 27.5 G needle and pelleted at 21,000xg for 10m at 4° C. 100 µg of protein was then added to 100 µl of prewashed HaloLink resin (Promega G1914), which was prepared by washing and pelleting for 2m at 800xg 3x in wash buffer (100 mM Tris pH 7.5, 150 mM NaCl, 1 mg/ml BSA, 0.005% IGPAL). Sufficient wash buffer was added to ensure an equal volume for all conditions (~400 µl), and samples were incubated on a tube rotator for 30m at room temperature. Samples were then pelleted at 800xg for 2m, saving the supernatant. The beads were then washed 3x in wash buffer, and resuspended in elution buffer (1% SDS, 50 mM Tris-HCl pH 7.5) and 10x sample buffer (10% SDS, 20%

bioRxiv preprint doi: https://doi.org/10.1101/648477; this version posted May 24, 2019. The copyright holder for this preprint (which was not certified by peer review) is the author/funder. All rights reserved. No reuse allowed without permission.

glycerol, 0.0025% bromophenol blue, 100 mM EDTA, 1 M DTT, 20 mM Tris, pH 8). Samples were then boiled at 95° C for 10m, and loaded onto a 10% SDS-PAGE gel alongside 10 µg of input protein and a fixed volume of supernatant to assess binding efficiency. The gel was run at 120 V, and samples were then transferred at 100 V at 4°C onto an activated 2 um polyvinylidene difluoride (PVDF) membrane (Bio-Rad 1620177), blocked with 3% BSA in 0.2% Tween-20 (Sigma P9614) in Tris-buffered saline (TBST) for 1h, and blotted overnight at 4°C with primary antibody in 3% BSA in TBST (Supplemental Table 4). The following day, blots were washed in 3x in TBST, incubated at room temperature for 1h with donkey anti-mouse 680 RD (Li-Cor 926-68072) and donkey anti-rabbit 800 CW (Li-Cor 925-32213) secondary antibodies, both diluted 1:5,000 in 3% BSA in TBST. Following treatment with secondary antibody, blots were washed 3x in TBST, placed in Tris-buffered saline, and imaged using an Odyssey CLx Imaging System (LI-COR).

Differential solubility fractionation

HEK293T cells were transfected in a 6-well plate with 3 µg of DNA/well using Lipofectamine 2000 according to the manufacturer's instructions. Two days after transfection, cells were collected in PBS and pelleted at 21,000xg for 5m. Cells were then resuspended in RIPA buffer (Thermo Scientific 89900) with protease inhibitors (Roche 11836170001) and incubated on ice for 15m. Lysates were then sonicated at 80% amplitude with 5s on/5s off for a total of 2m using a Fisher Brand Model 505 Sonic Dismembrenator (ThermoFisher). Samples were centrifuged at 21,000xg for 15m at 4°C, after which the supernatant was removed and saved as the RIPA-soluble fraction. The RIPA-insoluble pellet was washed in RIPA once more and resuspended in urea buffer (7 M urea, 2 M thiourea, 4% CHAPS, 30 mM Tris, pH 8.5) and incubated on ice for 5m. Samples were then centrifuged at 21,000xg for 15m at 4°C, and the supernatant was saved as the RIPA-insoluble, urea-soluble fraction. The RIPA-soluble samples were quantified and 10-30 µg of protein/well was diluted in RIPA buffer with 10x sample buffer. For urea fractions, equal volumes of each sample across conditions was diluted in urea buffer and 10x sample buffer. The RIPA-

bioRxiv preprint doi: https://doi.org/10.1101/648477; this version posted May 24, 2019. The copyright holder for this preprint (which was not certified by peer review) is the author/funder. All rights reserved. No reuse allowed without permission.

soluble samples were boiled for 10m before 10-30 µg of all samples were loaded onto a 10% SDS-PAGE gel with stacking gel and run at 120 V. The blot was then transferred and probed as described above.

Immunohistochemistry in human tissue

Paraffin-embedded human cortex and spinal cord obtained from the University of Michigan Brain Bank were cut into 5 µm thick sections and mounted on glass slides. Tissue samples were photobleached prior to immunofluorescence[132]. Briefly, slides were placed on ice, under a 7 Band Spectrum LED Light (HTG Supply 432W HTG-432-3W-7X) at 4°C for 12h. Slides were deparaffinized at 65°C for 20m, and rehydrated 5m sequentially in xylene (Fisher X3S-4), 100% ethanol (Fisher 3.8L), 95% ethanol, 70% ethanol, 50% ethanol, and PBS. Slides were then permeabilized with 0.1% Triton X-100 in PBS, and treated with 10 mM glycine in PBS. They were then incubated in a blocking solution (0.1% Triton X-100, 2% fetal calf serum, and 3% BSA in PBS) at room temperature for 1h before incubation overnight at 4°C in primary antibody diluted in blocking buffer (Supplemental Table 4). Slides were then washed 3x in PBS and incubated at room temperature with Alexa Fluor 488 goat anti-rabbit (Life Technologies A11034), Alexa Fluor goat anti-mouse 594 (Life Technologies A11032), and/or Alexa Fluor goat anti-chicken 647 (Life Technologies A21449) secondary antibody diluted 1:5000 in blocking solution for 1h. Following 3x washes in PBS containing 1:10,000 Hoechst 33258 dye (Invitrogen H3569), slides were mounted in mounting media (Fisher SP15-500) and allowed to dry in the dark overnight before being imaged the following day. Images were acquired using a Nikon Microphot-FXA microscope (Nikon, 1985) in combination with a 60x oil-immersion objective, a QIClick CCD Camera (Q Imaging, 7400-82-A1), and an X-Cite Series 120 light source (Lumen Dynamics).

Statistical analysis

bioRxiv preprint doi: https://doi.org/10.1101/648477; this version posted May 24, 2019. The copyright holder for this preprint (which was not certified by peer review) is the author/funder. All rights reserved. No reuse allowed without permission.

Statistical analyses were performed in R or Graphpad Prism 7. For primary neuron survival analysis, the open-source R survival package was used to determine hazard ratios describing the relative survival between conditions through Cox proportional hazards analysis[70]. Significance determined via the two-tailed t-test was used to assess differences between treatment groups for neuronal activity and transcript abundance via RT-PCR. The Kolmogorov-Smirnov test was used to assess differences between the distribution of TDP43 abundance in neurons under different activity conditions. One-way ANOVA with Tukey's or Dunnett's post-tests were used to assess significant differences among nuclear/cytoplasmic ratios, binding affinity, TDP43 splicing activity, and TDP43 autoregulation. Data are shown as mean ± SEM unless otherwise stated.

Ethics statement

All vertebrate animal work was approved by the Committee on the Use and Care of Animals (UCUCA) at the University of Michigan and in accordance with the United Kingdom Animals Act (1986). All experiments were performed in accordance with UCUCA guidelines. Rats (*Rattus norvegicus*) used for primary neuron collection were housed singly in chambers equipped with environmental enrichment. All studies were designed to minimize animal use. Rats were cared for by the Unit for Laboratory Animal Medicine at the University of Michigan; all individuals were trained and approved in the care and long-term maintenance of rodent colonies, in accordance with the NIH-supported Guide for the Care and Use of Laboratory Animals. All personnel handling the rats and administering euthanasia were properly trained in accordance with the UM Policy for Education and Training of Animal Care and Use Personnel. Euthanasia was fully consistent with the recommendations of the Guidelines on Euthanasia of the American Veterinary Medical Association.

bioRxiv preprint doi: https://doi.org/10.1101/648477; this version posted May 24, 2019. The copyright holder for this preprint (which was not certified by peer review) is the author/funder. All rights reserved. No reuse allowed without permission.

Declaration of Interests

The authors declare no competing interests.

Acknowledgements

This work was supported by National Institutes of Health (NIH), National Institute for Neurological Disorders and Stroke (NINDS) R01-NS097542, National Institute for Aging (NIA) P30 AG053760 (SJB), the University of Michigan Protein Folding Disease Initiative, and Ann Arbor Active Against ALS. We thank Dr. M. Uhler for advice, protocols and reagents; Drs. M. Ward and Y. Ayala for reagents; and Dr. J. Parent, Mr. M. Malik, and Mr. M. McMillian for their suggestions. We also thank Mr. M. Perkins from the Michigan Brain Bank (5P30 AG053760, University of Michigan Alzheimer's Disease Core Center), the Michigan ALS Biorepository, the University of Michigan DNA Sequencing Core, and the University of Michigan Department of Pharmacology for access to their confocal microscopy core. Finally, we thank those that donated the fibroblast and tissue samples that made these studies possible.

Author Contributions

K.W. was responsible for conceptualization, methodology, investigation, formal analysis, writing and visualization. S.J.B. contributed to conceptualization, methodology, formal analysis, writing, visualization, supervision, project administration, and funding acquisition. E.M.T. contributed to conceptualization and methodology, and R.M. was responsible for software. M.A.W. and N.B.G. contributed to data curation and formal analysis. J.S. contributed to supervision and project administration. Z.L., C.M.G., and A.S. contributed to investigation.

bioRxiv preprint doi: https://doi.org/10.1101/648477; this version posted May 24, 2019. The copyright holder for this preprint (which was not certified by peer review) is the author/funder. All rights reserved. No reuse allowed without permission.

Figure Legends

Figure 1. Hyperexcitability drives TDP43 accumulation in human iNeurons.

(**A**) Schematic of the cassette used to integrate Ngn1 and Ngn2 into the *CLYBL* safe harbor locus under a doxycycline-inducible (Tet-on) promoter. CLYBL, targeting sequence; Puro, puromycin resistance gene; pA, poly-A tail; P1,P2, promoters; RFP, mCherry; rtTA, reverse tetracycline-controlled transactivator; Ngn1,2, Neurogenin1 and 2; T2A, self-cleaving peptide; TRE, tetracycline response element. (**B**) Timeline depicting the differentiation of iPSCs into forebrain-like neurons within 2w of doxycycline addition. (**C**) The resultant neurons are RFP-positive and express the neuronal markers Vglut1 and Tuj1. (**D**) Spontaneous neuronal activity visualized by the Ca^{2+} reporter gCaMP6f at 2w. Activity was pharmacologically modulated with bath application of glutamate or TTX. Vehicle n=257, Glutamate n=327, TTX n=403, stratified among 3 replicates; ****$p<0.0001$, one-way ANOVA with Dunnett's post-test. (**E**) Treatment with TEA significantly increased neuronal activity. Vehicle n= 312, TEA n=369, stratified among 3 replicates, **** $p<0.0001$, two-tailed t-test. (**F**) Example traces depicting changes in gCaMP6f fluorescence for each condition. (**G**) Heat maps depicting global changes in activity. Each row represents one neuron, and each column represents a 20s observation window. Thirty intervals were collected over a 12h period. Box color indicates the relative firing rate of each cell at each timepoint ranging from low (blue) to high (red). (**H**) N-terminal TDP43 immunoreactivity was increased in TEA-treated iNeurons and decreased in TTX-treated iNeurons (TTX), indicating a bidirectional relationship between activity and TDP43 abundance. (**I**) Density plot depicting the change in TDP43 immunoreactivity between conditions. Vehicle n=110, TEA n=113, TTX n=96, 2 replicates, dashes indicate single neurons, *$p<0.01$, Kolmogorov-Smirnov test. (**J**) No such relationship was identified when TDP43 abundance is detected using an antibody directed against the C-terminus.

bioRxiv preprint doi: https://doi.org/10.1101/648477; this version posted May 24, 2019. The copyright holder for this preprint (which was not certified by peer review) is the author/funder. All rights reserved. No reuse allowed without permission.

(**K**) Density plot depicting the change in C-terminal TDP43 immunoreactivity between conditions. Vehicle n=187, TEA n=541, TTX n=443, 2 replicates, dashes indicate single neurons, not significant by the Kolmogorov-Smirnov test. Scale bars in (**C**), 50 µm top, 20 µm bottom. Scale bars in (**H**), (**J**), 20 µm.

Figure 2. TDP43 species harboring the N- but not the C-terminus are regulated by neuronal activity.

(**A**) Strategy for labeling native TDP43 in human iPSC-derived neurons using CRISPR/Cas9. Dendra2 (D2, green) was inserted 3' to the *TARDBP* start codon (green arrow) or 5' to the conventional stop codon (red arrow), enabling fluorescent labeling of the TDP43 N- or C-terminus, respectively. In iNeurons, N-terminally tagged TDP43 (**B**, D2-TDP43) appeared both nuclear and cytoplasmic in distribution, while C-terminally tagged TDP43 (**C**, TDP43-D2) was primarily nuclear. (**D**) Density plot depicting the fluorescence intensity of D2-TDP43 upon application of vehicle (n=158), TEA (n=250), or TTX (n=221). (**E**) Density plot depicting the fluorescence intensity of TDP43-D2 with addition of vehicle (n=96), TEA (n=145), or TTX (n=98). In (**D**) and (**E**), dashes indicate individual neurons from 2 replicates, **p<0.01, ****p<0.0001, Kolmogorov-Smirnov test. Scale bars in (**B**) and (**C**), 20 µm.

Figure 3. Hyperactivity drives alternative splicing of *TARDBP.*

(**A**) Sashimi plot depicting splicing events for the *TARDBP* gene, assembled from HEK293T cell RNA-seq data[59]. Splicing events predicted to skip the majority of exon 6—encoding the TDP43 C-terminus—are highlighted in black. (**B**) Schematic of transcripts predicted to result in full-length (fl) TDP43 and C-terminally shortened (s) TDP43. Green triangles indicate start codons, red triangles indicate stop codons, and PCR primers are color-coded. (**C**) qRT-PCR of human iNeurons treated with TEA, showing activity dependent upregulation of total and sTDP43. ARC (activity related cytoskeleton associated protein) acts as a positive control for activity-dependent

bioRxiv preprint doi: https://doi.org/10.1101/648477; this version posted May 24, 2019. The copyright holder for this preprint (which was not certified by peer review) is the author/funder. All rights reserved. No reuse allowed without permission.

gene regulation. PCR products corresponding to each primer pair are shown below. Data were combined from 3 replicates, **p<0.01, ***p<0.001, ****p<0.0001, two-tailed t-test. (**D**) Schematic comparing flTDP43 and sTDP43 proteins. Novel sTDP43 C-terminus is shown in purple; NLS, nuclear localization signal; RRM, RNA recognition motif; GRD, glycine rich domain.

Figure 4. sTDP43 accumulates within the cytosol due to a putative NES.

(**A**) Rat primary mixed cortical neurons were transfected with mApple and EGFP-tagged TDP43 isoforms, then imaged by fluorescence microscopy. (**B**) Amino acid sequence of the sTDP43 tail includes a putative NES identified through predictive software NetNES 1.1. Light blue, polar; purple, positively charged; green, hydrophobic residues. (**C**) sTDP43-EGFP was significantly more cytosolic in distribution compared to flTDP43-EGFP, while mutation of the putative NES (mNES) restores nuclear localization. EGFP n=481, flTDP43-EGFP n=385, sTDP43-EGFP n=456, sTDP43(mNES)-EGFP n=490, stratified among 3 replicates, ****p<0.0001, one-way ANOVA with Dunnett's post-test. (**D**) Rat primary mixed cortical neurons were transfected with EGFP or EGFP fused to either the novel C-terminal tail of sTDP43 or a tail harboring a mutated NES (mNES). (**E**) The C-terminal sTDP43 tail is sufficient to significantly mislocalize EGFP to the cytosol, and mislocalization depends on the NES. Shuttle-RFP, a construct with a strong NES, serves as a positive control for a cytosolic protein. EGFP n=2490, Shuttle-RFP n=2073, EGFP-tail n=1956, EGFP-tail(mNES) n=2482, stratified among 3 replicates, ****p<0.0001, one-way ANOVA with Dunnett's post-test. Scale bars in (**A**) and (**D**), 20 µm.

Figure 5. sTDP43 overexpression is neurotoxic.

(**A**) Example of a single neuron expressing mApple and sTDP43-EGFP, tracked by longitudinal fluorescence microscopy. Fragmentation of the cell body and loss of fluorescence on Day 5 indicates cell death. (**B**) The risk of death was significantly greater in neurons overexpressing sTDP43-EGFP and flTDP43-EGFP, in comparison to those expressing EGFP alone. EGFP n=

bioRxiv preprint doi: https://doi.org/10.1101/648477; this version posted May 24, 2019. The copyright holder for this preprint (which was not certified by peer review) is the author/funder. All rights reserved. No reuse allowed without permission.

869, flTDP43-EGFP n=708, sTDP43-EGFP n=732, stratified among 3 replicates, ***$p<2x10^{-16}$, Cox proportional hazards analysis. Scale bar in (**A**), 20 µm.

Figure 6. sTDP43 overexpression leads to the cytoplasmic deposition and nuclear clearance of endogenous TDP43.

(**A**) Halo-tagged flTDP43 or sTDP43 were expressed in HEK293T cells and immunoprecipitated with HaloLink. Bound TDP43 was immunoblotted with a C-terminal TDP43 antibody. GAPDH served as a loading control. Input, (I); eluate, (E). (**B**) Quantification of data shown in (A), demonstrating the fraction of total TDP43 bound to flTDP43-Halo, sTDP43-Halo, or Halo alone. Data was combined from 3 replicates, *p<0.05, **p<0.01, one-way ANOVA with Dunnett's post-test. (**C**) HEK293T cells were transfected with EGFP or EGFP-tagged sTDP43, then immunostained using an antibody that recognizes the C-terminus of endogenous (Endo) TDP43. Red, nuclear regions of interest (ROIs) determined by DAPI staining. (**D**) Nuclear, endogenous TDP43 is reduced by sTDP43 overexpression in HEK293T cells. EGFP n=1537, sTDP43-EGFP n=1997, 3 replicates, ****p<0.0001, two-tailed t-test. (**E**) Cytoplasmic endogenous TDP43 is elevated by sTDP43 overexpression in HEK293T cells. EGFP n=129, sTDP43-EGFP n=113, 3 replicates, ****p<0.0001, two-tailed t-test. (**F**) Primary mixed rat cortical neurons were transfected with EGFP or EGFP-tagged sTDP43, then immunostained using a C-terminal TDP43 antibody. Red, nuclear ROIs determined by DAPI staining. (**G**) sTDP43 overexpression resulted in a significant drop in nuclear, endogenous TDP43 in primary neurons (EGFP n=395, EGFP-sTDP43 n=323, 3 replicates, ****p<0.0001, two-tailed t-test), but this was not accompanied by increases in cytoplasmic, endogenous TDP43 (**H**) (EGFP=394, EGFP-sTDP43=323, 3 replicates, ns by two-tailed t-test). Scale bar in (**C**), (**F**) 20 µm.

Figure 7. sTDP43 transcripts are enriched in lumbar motor neurons.

bioRxiv preprint doi: https://doi.org/10.1101/648477; this version posted May 24, 2019. The copyright holder for this preprint (which was not certified by peer review) is the author/funder. All rights reserved. No reuse allowed without permission.

(**A**) Sashimi plots depicting *TARDBP* splicing in murine frontal cortex homogenate (red) or microdissected lumbar motor neurons (blue). (**B**) Both sTDP43-1 and sTDP43-2 splice events are highly enriched in lumbar motor neurons compared to frontal cortex homogenate. Graph depicts read counts normalized to reads per million for each library (4 replicates, ****p<0.0001 multiple t-test with the Holm-Sidak correction). (**C**) While sTDP43-1 and -2 each comprise ~1% of the total *TARDBP* transcripts in frontal cortex homogenate, they make up 17 and 22% of total *TARDBP* transcripts in lumbar motor neurons, respectively (frontal cortex n=6, lumbar motor neurons n=4, *p<0.05, **p<0.01, ***p<0.001, two-way ANOVA with Sidak's multiple comparison test). (**D**) sTDP43-1 is enriched within lumbar motor neurons microdissected from both control (n=9) and sALS (n=13) patient tissue. (**E**) sTDP43-1 makes up the majority of total *TARDBP* transcripts in both control and sALS patient lumbar motor neurons.

Figure 8. Endogenous sTDP43 is detectable *in vivo* by antibodies generated against its novel C-terminus.

(**A**) The sTDP43 antibody specifically recognizes EGFP fused to the 18-amino acid C-terminus of sTDP43, but not EGFP alone. Preincubation with a peptide corresponding to the sTDP43 C-terminal tail abolishes the signal. (**B**) Western blot of EGFP-tagged flTDP43 or sTDP43 overexpressed in HEK293T cells, demonstrating the insolubility of sTDP43 in RIPA buffer. Black arrowhead, endogenous TDP43; white arrowhead EGFP-flTDP43. (**C**) ICC using sTDP43 antibodies showed increased immunoreactivity in TEA-treated iNeurons and decreased immunoreactivity in TTX-treated iNeurons. (**D**) Density plot depicting the change in sTDP43 immunoreactivity between conditions. Vehicle n=300, TEA n=354, TTX n=333, 3 replicates, dashes indicate single neurons, * p<0.05, **** p<0.0001, Kolmogorov-Smirnov test. (**E**) IHC comparing the distribution of N-terminal TDP43 and sTDP43 in spinal cord and cortex from patients with sporadic (s)ALS and controls. (**F**) IHC demonstrating neuronal and glial sTDP43

bioRxiv preprint doi: https://doi.org/10.1101/648477; this version posted May 24, 2019. The copyright holder for this preprint (which was not certified by peer review) is the author/funder. All rights reserved. No reuse allowed without permission.

accumulation in cortex from individuals with sALS and controls. Scale bars in (**C**), (**E**), and (**F**) 20 µm.

References

1. Bruijn, L. I., Miller, T. M. & Cleveland, D. W. Unraveling the mechanisms involved in motor neuron degeneration in ALS. *Annu. Rev. Neurosci.* **27**, 723–749 (2004).
2. Neumann, M. Molecular neuropathology of TDP-43 proteinopathies. *Int. J. Mol. Sci.* **10**, 232–246 (2009).
3. Murray, M. E. *et al.* Clinical and neuropathologic heterogeneity of c9FTD/ALS associated with hexanucleotide repeat expansion in C9ORF72. *Acta Neuropathol.* **122**, 673–690 (2011).
4. Seilhean, D. *et al.* Accumulation of TDP-43 and α-actin in an amyotrophic lateral sclerosis patient with the K17I ANG mutation. *Acta Neuropathol.* **118**, 561–573 (2009).
5. Van Mossevelde, S. *et al.* Clinical features of TBK1 carriers compared with C9orf72, GRN and non-mutation carriers in a Belgian cohort. *Brain* **139**, 452–467 (2016).
6. Smith, B. N. *et al.* Novel mutations support a role for Profilin 1 in the pathogenesis of ALS. *Neurobiol. Aging* **36**, 1602.e17–27 (2015).
7. Deng, H.-X. *et al.* Mutations in UBQLN2 cause dominant X-linked juvenile and adult-onset ALS and ALS/dementia. *Nature* **477**, 211–215 (2011).
8. Johnson, J. O. *et al.* Exome sequencing reveals VCP mutations as a cause of familial ALS. *Neuron* **68**, 857–864 (2010).
9. Kim, H. J. *et al.* Mutations in prion-like domains in hnRNPA2B1 and hnRNPA1 cause multisystem proteinopathy and ALS. *Nature* **495**, 467–473 (2013).
10. Kraemer, B. C. *et al.* Loss of murine TDP-43 disrupts motor function and plays an essential

bioRxiv preprint doi: https://doi.org/10.1101/648477; this version posted May 24, 2019. The copyright holder for this preprint (which was not certified by peer review) is the author/funder. All rights reserved. No reuse allowed without permission.

role in embryogenesis. *Acta Neuropathol.* **119**, 409–419 (2010).

11. Wu, L.-S., Cheng, W.-C. & Shen, C.-K. J. Targeted depletion of TDP-43 expression in the spinal cord motor neurons leads to the development of amyotrophic lateral sclerosis-like phenotypes in mice. *J. Biol. Chem.* **287**, 27335–27344 (2012).
12. Iguchi, Y. *et al.* Loss of TDP-43 causes age-dependent progressive motor neuron degeneration. *Brain* **136**, 1371–1382 (2013).
13. Sephton, C. F. *et al.* TDP-43 is a developmentally regulated protein essential for early embryonic development. *J. Biol. Chem.* **285**, 6826–6834 (2010).
14. Barmada, S. J. *et al.* Cytoplasmic mislocalization of TDP-43 is toxic to neurons and enhanced by a mutation associated with familial amyotrophic lateral sclerosis. *J. Neurosci.* **30**, 639–649 (2010).
15. Archbold, H. C. *et al.* TDP43 nuclear export and neurodegeneration in models of amyotrophic lateral sclerosis and frontotemporal dementia. *Sci. Rep.* **8**, 4606 (2018).
16. Swarup, V. *et al.* Pathological hallmarks of amyotrophic lateral sclerosis/frontotemporal lobar degeneration in transgenic mice produced with TDP-43 genomic fragments. *Brain* **134**, 2610–2626 (2011).
17. Wils, H. *et al.* TDP-43 transgenic mice develop spastic paralysis and neuronal inclusions characteristic of ALS and frontotemporal lobar degeneration. *Proc. Natl. Acad. Sci. U. S. A.* **107**, 3858–3863 (2010).
18. Dayton, R. D. *et al.* Selective forelimb impairment in rats expressing a pathological TDP-43 25 kDa C-terminal fragment to mimic amyotrophic lateral sclerosis. *Mol. Ther.* **21**, 1324–1334 (2013).
19. Tatom, J. B. *et al.* Mimicking aspects of frontotemporal lobar degeneration and Lou Gehrig's disease in rats via TDP-43 overexpression. *Mol. Ther.* **17**, 607–613 (2009).
20. Voigt, A. *et al.* TDP-43-mediated neuron loss in vivo requires RNA-binding activity. *PLoS One* **5**, e12247 (2010).

bioRxiv preprint doi: https://doi.org/10.1101/648477; this version posted May 24, 2019. The copyright holder for this preprint (which was not certified by peer review) is the author/funder. All rights reserved. No reuse allowed without permission.

21. Li, Y. *et al.* A Drosophila model for TDP-43 proteinopathy. *Proc. Natl. Acad. Sci. U. S. A.* **107**, 3169–3174 (2010).

22. Kabashi, E. *et al.* Gain and loss of function of ALS-related mutations of TARDBP (TDP-43) cause motor deficits in vivo. *Hum. Mol. Genet.* **19**, 671–683 (2010).

23. Schmid, B. *et al.* Loss of ALS-associated TDP-43 in zebrafish causes muscle degeneration, vascular dysfunction, and reduced motor neuron axon outgrowth. *Proc. Natl. Acad. Sci. U. S. A.* **110**, 4986–4991 (2013).

24. Uchida, A. *et al.* Non-human primate model of amyotrophic lateral sclerosis with cytoplasmic mislocalization of TDP-43. *Brain* **135**, 833–846 (2012).

25. Jackson, K. L. *et al.* Initial gene vector dosing for studying symptomatology of amyotrophic lateral sclerosis in non-human primates. *J. Med. Primatol.* **44**, 66–75 (2015).

26. Vucic, S., Nicholson, G. A. & Kiernan, M. C. Cortical hyperexcitability may precede the onset of familial amyotrophic lateral sclerosis. *Brain* **131**, 1540–1550 (2008).

27. Kanai, K., Shibuya, K. & Kuwabara, S. Motor axonal excitability properties are strong predictors for survival in amyotrophic lateral sclerosis. *Rinsho Shinkeigaku* **51**, 1118–1119 (2011).

28. Kanai, K. *et al.* Altered axonal excitability properties in amyotrophic lateral sclerosis: impaired potassium channel function related to disease stage. *Brain* **129**, 953–962 (2006).

29. Enterzari-Taher, M., Eisen, A., Stewart, H. & Nakajima, M. Abnormalities of cortical inhibitory neurons in amyotrophic lateral sclerosis. *Muscle Nerve* **20**, 65–71 (1997).

30. Zanette, G. *et al.* Different mechanisms contribute to motor cortex hyperexcitability in amyotrophic lateral sclerosis. *Clin. Neurophysiol.* **113**, 1688–1697 (2002).

31. Geevasinga, N. *et al.* Cortical Function in Asymptomatic Carriers and Patients With C9orf72 Amyotrophic Lateral Sclerosis. *JAMA Neurol.* **72**, 1268–1274 (2015).

32. Vucic, S., Cheah, B. C. & Kiernan, M. C. Defining the mechanisms that underlie cortical hyperexcitability in amyotrophic lateral sclerosis. *Exp. Neurol.* **220**, 177–182 (2009).

bioRxiv preprint doi: https://doi.org/10.1101/648477; this version posted May 24, 2019. The copyright holder for this preprint (which was not certified by peer review) is the author/funder. All rights reserved. No reuse allowed without permission.

33. Karandreas, N. *et al.* Impaired interhemispheric inhibition in amyotrophic lateral sclerosis. *Amyotroph. Lateral Scler.* **8**, 112–118 (2007).

34. Tamura, N. *et al.* Increased nodal persistent Na currents in human neuropathy and motor neuron disease estimated by latent addition. *Clinical Neurophysiology* **117**, 2451–2458 (2006).

35. Shibuya, K. *et al.* Markedly reduced axonal potassium channel expression in human sporadic amyotrophic lateral sclerosis: An immunohistochemical study. *Experimental Neurology* **232**, 149–153 (2011).

36. Geevasinga, N. *et al.* Riluzole exerts transient modulating effects on cortical and axonal hyperexcitability in ALS. *Amyotroph. Lateral Scler. Frontotemporal Degener.* **17**, 580–588 (2016).

37. Kuo, J. J. *et al.* Hyperexcitability of cultured spinal motoneurons from presymptomatic ALS mice. *J. Neurophysiol.* **91**, 571–575 (2004).

38. Pieri, M. *et al.* Altered excitability of motor neurons in a transgenic mouse model of familial amyotrophic lateral sclerosis. *Neurosci. Lett.* **351**, 153–156 (2003).

39. Van Zundert, B. *et al.* Neonatal neuronal circuitry shows hyperexcitable disturbance in a mouse model of the adult-onset neurodegenerative disease amyotrophic lateral sclerosis. *Journal of Neuroscience* **28**, 10864–10874 (2008).

40. Saba, L. *et al.* Altered Functionality, Morphology, and Vesicular Glutamate Transporter Expression of Cortical Motor Neurons from a Presymptomatic Mouse Model of Amyotrophic Lateral Sclerosis. *Cerebral Cortex* **26**, 1512–1528 (2016).

41. Pieri, M., Carunchio, I., Curcio, L., Mercuri, N. B. & Zona, C. Increased persistent sodium current determines cortical hyperexcitability in a genetic model of amyotrophic lateral sclerosis. *Exp. Neurol.* **215**, 368–379 (2009).

42. Wainger, B. J. *et al.* Intrinsic membrane hyperexcitability of amyotrophic lateral sclerosis patient-derived motor neurons. *Cell Rep.* **7**, 1–11 (2014).

bioRxiv preprint doi: https://doi.org/10.1101/648477; this version posted May 24, 2019. The copyright holder for this preprint (which was not certified by peer review) is the author/funder. All rights reserved. No reuse allowed without permission.

43. Devlin, A.-C. *et al.* Human iPSC-derived motoneurons harbouring TARDBP or C9ORF72 ALS mutations are dysfunctional despite maintaining viability. *Nat. Commun.* **6**, 5999 (2015).

44. Sareen, D. *et al.* Targeting RNA foci in iPSC-derived motor neurons from ALS patients with a C9ORF72 repeat expansion. *Sci. Transl. Med.* **5**, 208ra149 (2013).

45. Zhang, Y. *et al.* Rapid single-step induction of functional neurons from human pluripotent stem cells. *Neuron* **78**, 785–798 (2013).

46. Lam, R. S., Töpfer, F. M., Wood, P. G., Busskamp, V. & Bamberg, E. Functional Maturation of Human Stem Cell-Derived Neurons in Long-Term Cultures. *PLoS One* **12**, e0169506 (2017).

47. Busskamp, V. *et al.* Rapid neurogenesis through transcriptional activation in human stem cells. *Mol. Syst. Biol.* **10**, 760 (2014).

48. Gupta, S. *et al.* Fibroblast growth factor 2 regulates activity and gene expression of human post-mitotic excitatory neurons. *J. Neurochem.* **145**, 188–203 (2018).

49. Wang, I.-F., Wu, L.-S., Chang, H.-Y. & Shen, C.-K. J. TDP-43, the signature protein of FTLD-U, is a neuronal activity-responsive factor. *J. Neurochem.* **105**, 797–806 (2008).

50. Schwenk, B. M. *et al.* TDP-43 loss of function inhibits endosomal trafficking and alters trophic signaling in neurons. *The EMBO Journal* **35**, 2350–2370 (2016).

51. Gopal, P. P., Nirschl, J. J., Klinman, E. & Holzbaur, E. L. F. Amyotrophic lateral sclerosis-linked mutations increase the viscosity of liquid-like TDP-43 RNP granules in neurons. *Proc. Natl. Acad. Sci. U. S. A.* **114**, E2466–E2475 (2017).

52. Zhang, Y.-J. *et al.* The dual functions of the extreme N-terminus of TDP-43 in regulating its biological activity and inclusion formation. *Hum. Mol. Genet.* **22**, 3112–3122 (2013).

53. Suzuki, H., Shibagaki, Y., Hattori, S. & Matsuoka, M. Nuclear TDP-43 causes neuronal toxicity by escaping from the inhibitory regulation by hnRNPs. *Hum. Mol. Genet.* **24**, 1513–1527 (2015).

bioRxiv preprint doi: https://doi.org/10.1101/648477; this version posted May 24, 2019. The copyright holder for this preprint (which was not certified by peer review) is the author/funder. All rights reserved. No reuse allowed without permission.

54. Baker, M. Reproducibility crisis: Blame it on the antibodies. *Nature* **521**, 274–276 (2015).

55. Begley, C. G. & Ellis, L. M. Drug development: Raise standards for preclinical cancer research. *Nature* **483**, 531–533 (2012).

56. Ran, F. A. *et al.* Double nicking by RNA-guided CRISPR Cas9 for enhanced genome editing specificity. *Cell* **154**, 1380–1389 (2013).

57. Eom, T. *et al.* NOVA-dependent regulation of cryptic NMD exons controls synaptic protein levels after seizure. *Elife* **2**, e00178 (2013).

58. Kolisnyk, B. *et al.* Cholinergic Regulation of hnRNPA2/B1 Translation by M1 Muscarinic Receptors. *J. Neurosci.* **36**, 6287–6296 (2016).

59. Flores, B. N. *et al.* An Intramolecular Salt Bridge Linking TDP43 RNA Binding, Protein Stability, and TDP43-Dependent Neurodegeneration. *Cell Rep.* **27**, 1133–1150.e8 (2019).

60. Wang, H.-Y., Wang, I.-F., Bose, J. & Shen, C.-K. J. Structural diversity and functional implications of the eukaryotic TDP gene family. *Genomics* **83**, 130–139 (2004).

61. D'Alton, S., Altshuler, M. & Lewis, J. Studies of alternative isoforms provide insight into TDP-43 autoregulation and pathogenesis. *RNA* **21**, 1419–1432 (2015).

62. Avendaño-Vázquez, S. E. *et al.* Autoregulation of TDP-43 mRNA levels involves interplay between transcription, splicing, and alternative polyA site selection. *Genes Dev.* **26**, 1679–1684 (2012).

63. Bembich, S. *et al.* Predominance of spliceosomal complex formation over polyadenylation site selection in TDP-43 autoregulation. *Nucleic Acids Res.* **42**, 3362–3371 (2014).

64. Seyfried, N. T. *et al.* Multiplex SILAC analysis of a cellular TDP-43 proteinopathy model reveals protein inclusions associated with SUMOylation and diverse polyubiquitin chains. *Mol. Cell. Proteomics* **9**, 705–718 (2010).

65. Dammer, E. B. *et al.* Coaggregation of RNA-binding proteins in a model of TDP-43 proteinopathy with selective RGG motif methylation and a role for RRM1 ubiquitination. *PLoS One* **7**, e38658 (2012).

bioRxiv preprint doi: https://doi.org/10.1101/648477; this version posted May 24, 2019. The copyright holder for this preprint (which was not certified by peer review) is the author/funder. All rights reserved. No reuse allowed without permission.

66. la Cour, T. *et al.* Analysis and prediction of leucine-rich nuclear export signals. *Protein Eng. Des. Sel.* **17**, 527–536 (2004).

67. Niopek, D., Wehler, P., Roensch, J., Eils, R. & Di Ventura, B. Optogenetic control of nuclear protein export. *Nature Communications* **7**, (2016).

68. Barmada, S. J. *et al.* Amelioration of toxicity in neuronal models of amyotrophic lateral sclerosis by hUPF1. *Proc. Natl. Acad. Sci. U. S. A.* **112**, 7821–7826 (2015).

69. Malik, A. M. *et al.* Matrin 3-dependent neurotoxicity is modified by nucleic acid binding and nucleocytoplasmic localization. *Elife* **7**, (2018).

70. Weskamp, K., Safren, N., Miguez, R. & Barmada, S. Monitoring Neuronal Survival via Longitudinal Fluorescence Microscopy. *JoVE (Journal of Visualized Experiments)* e59036 (2019).

71. Christensen, E. Multivariate survival analysis using Cox's regression model. *Hepatology* **7**, 1346–1358 (1987).

72. Afroz, T. *et al.* Functional and dynamic polymerization of the ALS-linked protein TDP-43 antagonizes its pathologic aggregation. *Nature Communications* **8**, (2017).

73. Kuo, P.-H., Doudeva, L. G., Wang, Y.-T., Shen, C.-K. J. & Yuan, H. S. Structural insights into TDP-43 in nucleic-acid binding and domain interactions. *Nucleic Acids Res.* **37**, 1799–1808 (2009).

74. Johnson, B. S. *et al.* TDP-43 is intrinsically aggregation-prone, and amyotrophic lateral sclerosis-linked mutations accelerate aggregation and increase toxicity. *J. Biol. Chem.* **284**, 20329–20339 (2009).

75. Zhang, Y.-J. *et al.* Aberrant cleavage of TDP-43 enhances aggregation and cellular toxicity. *Proc. Natl. Acad. Sci. U. S. A.* **106**, 7607–7612 (2009).

76. Bozzo, F. *et al.* Structural insights into the multi-determinant aggregation of TDP-43 in motor neuron-like cells. *Neurobiol. Dis.* **94**, 63–72 (2016).

77. Budini, M., Romano, V., Quadri, Z., Buratti, E. & Baralle, F. E. TDP-43 loss of cellular

bioRxiv preprint doi: https://doi.org/10.1101/648477; this version posted May 24, 2019. The copyright holder for this preprint (which was not certified by peer review) is the author/funder. All rights reserved. No reuse allowed without permission.

function through aggregation requires additional structural determinants beyond its C-terminal Q/N prion-like domain. *Hum. Mol. Genet.* **24**, 9–20 (2015).

78. Chang, C.-K. *et al.* The N-terminus of TDP-43 promotes its oligomerization and enhances DNA binding affinity. *Biochem. Biophys. Res. Commun.* **425**, 219–224 (2012).
79. Ayala, Y. M., Pagani, F. & Baralle, F. E. TDP43 depletion rescues aberrant CFTR exon 9 skipping. *FEBS Lett.* **580**, 1339–1344 (2006).
80. Buratti, E. *et al.* Nuclear factor TDP-43 and SR proteins promote in vitro and in vivo CFTR exon 9 skipping. *EMBO J.* **20**, 1774–1784 (2001).
81. Polymenidou, M. *et al.* Long pre-mRNA depletion and RNA missplicing contribute to neuronal vulnerability from loss of TDP-43. *Nat. Neurosci.* **14**, 459–468 (2011).
82. Ayala, Y. M. *et al.* TDP-43 regulates its mRNA levels through a negative feedback loop. *EMBO J.* **30**, 277–288 (2011).
83. White, M. A. *et al.* TDP-43 gains function due to perturbed autoregulation in a Tardbp knock-in mouse model of ALS-FTD. *Nat. Neurosci.* **21**, 552–563 (2018).
84. Krach, F. *et al.* Transcriptome–pathology correlation identifies interplay between TDP-43 and the expression of its kinase CK1E in sporadic ALS. *Acta Neuropathologica* **136**, 405–423 (2018).
85. D'Erchia, A. M. *et al.* Massive transcriptome sequencing of human spinal cord tissues provides new insights into motor neuron degeneration in ALS. *Sci. Rep.* **7**, 10046 (2017).
86. Prudencio, M. *et al.* Distinct brain transcriptome profiles in C9orf72-associated and sporadic ALS. *Nat. Neurosci.* **18**, 1175–1182 (2015).
87. Li, H.-R., Chiang, W.-C., Chou, P.-C., Wang, W.-J. & Huang, J.-R. TAR DNA-binding protein 43 (TDP-43) liquid–liquid phase separation is mediated by just a few aromatic residues. *J. Biol. Chem.* **293**, 6090–6098 (2018).
88. McGurk, L. *et al.* Poly(ADP-Ribose) Prevents Pathological Phase Separation of TDP-43 by Promoting Liquid Demixing and Stress Granule Localization. *Molecular Cell* **71**, 703–717.e9

bioRxiv preprint doi: https://doi.org/10.1101/648477; this version posted May 24, 2019. The copyright holder for this preprint (which was not certified by peer review) is the author/funder. All rights reserved. No reuse allowed without permission.

(2018).

89. Conicella, A. E., Zerze, G. H., Mittal, J. & Fawzi, N. L. ALS Mutations Disrupt Phase Separation Mediated by α-Helical Structure in the TDP-43 Low-Complexity C-Terminal Domain. *Structure* **24**, 1537–1549 (2016).
90. Mann, J. R. *et al.* RNA Binding Antagonizes Neurotoxic Phase Transitions of TDP-43. *Neuron* (2019). doi:10.1016/j.neuron.2019.01.048
91. Agrawal, S. *et al.* RNA recognition motifs of disease-linked RNA-binding proteins contribute to amyloid formation. *Sci. Rep.* **9**, 6171 (2019).
92. Franzmann, T. & Alberti, S. Prion-like low-complexity sequences: Key regulators of protein solubility and phase behavior. *J. Biol. Chem.* (2018). doi:10.1074/jbc.TM118.001190
93. Riback, J. A. *et al.* Stress-Triggered Phase Separation Is an Adaptive, Evolutionarily Tuned Response. *Cell* **168**, 1028–1040.e19 (2017).
94. Kroschwald, S. *et al.* Different Material States of Pub1 Condensates Define Distinct Modes of Stress Adaptation and Recovery. *Cell Rep.* **23**, 3327–3339 (2018).
95. Franzmann, T. M. *et al.* Phase separation of a yeast prion protein promotes cellular fitness. *Science* **359**, (2018).
96. Ayala, Y. M. *et al.* Human, Drosophila, and C.elegans TDP43: nucleic acid binding properties and splicing regulatory function. *J. Mol. Biol.* **348**, 575–588 (2005).
97. Johnson, B. S., McCaffery, J. M., Lindquist, S. & Gitler, A. D. A yeast TDP-43 proteinopathy model: Exploring the molecular determinants of TDP-43 aggregation and cellular toxicity. *Proc. Natl. Acad. Sci. U. S. A.* **105**, 6439–6444 (2008).
98. Wang, A., Conicella, A. E. & Schmidt, H. B. A single N-terminal phosphomimic disrupts TDP-43 polymerization, phase separation, and RNA splicing. *EMBO J.* (2018).
99. Leigh, P. N. *et al.* Ubiquitin-immunoreactive intraneuronal inclusions in amyotrophic lateral sclerosis. Morphology, distribution, and specificity. *Brain* **114 (Pt 2)**, 775–788 (1991).
100. Ravits, J., Paul, P. & Jorg, C. Focality of upper and lower motor neuron degeneration at the

bioRxiv preprint doi: https://doi.org/10.1101/648477; this version posted May 24, 2019. The copyright holder for this preprint (which was not certified by peer review) is the author/funder. All rights reserved. No reuse allowed without permission.

clinical onset of ALS. *Neurology* **68**, 1571–1575 (2007).

101. Udan, M. & Baloh, R. H. Implications of the prion-related Q/N domains in TDP-43 and FUS. *Prion* **5**, 1–5 (2011).

102. Furukawa, Y., Kaneko, K., Watanabe, S., Yamanaka, K. & Nukina, N. A seeding reaction recapitulates intracellular formation of Sarkosyl-insoluble transactivation response element (TAR) DNA-binding protein-43 inclusions. *J. Biol. Chem.* **286**, 18664–18672 (2011).

103. Nonaka, T., Kametani, F., Arai, T., Akiyama, H. & Hasegawa, M. Truncation and pathogenic mutations facilitate the formation of intracellular aggregates of TDP-43. *Hum. Mol. Genet.* **18**, 3353–3364 (2009).

104. Tsuji, H. *et al.* Molecular analysis and biochemical classification of TDP-43 proteinopathy. *Brain* **135**, 3380–3391 (2012).

105. Neumann, M. *et al.* Ubiquitinated TDP-43 in frontotemporal lobar degeneration and amyotrophic lateral sclerosis. *Science* **314**, 130–133 (2006).

106. Igaz, L. M. *et al.* Expression of TDP-43 C-terminal Fragments in Vitro Recapitulates Pathological Features of TDP-43 Proteinopathies. *J. Biol. Chem.* **284**, 8516–8524 (2009).

107. Wang, I.-F. *et al.* The self-interaction of native TDP-43 C terminus inhibits its degradation and contributes to early proteinopathies. *Nat. Commun.* **3**, 766 (2012).

108. Wang, Y.-T. *et al.* The truncated C-terminal RNA recognition motif of TDP-43 protein plays a key role in forming proteinaceous aggregates. *J. Biol. Chem.* **288**, 9049–9057 (2013).

109. Berning, B. A. & Walker, A. K. The Pathobiology of TDP-43 C-Terminal Fragments in ALS and FTLD. *Front. Neurosci.* **13**, 335 (2019).

110. Yamashita, T. *et al.* A role for calpain-dependent cleavage of TDP-43 in amyotrophic lateral sclerosis pathology. *Nat. Commun.* **3**, 1307 (2012).

111. Igaz, L. M. *et al.* Enrichment of C-Terminal Fragments in TAR DNA-Binding Protein-43 Cytoplasmic Inclusions in Brain but not in Spinal Cord of Frontotemporal Lobar Degeneration and Amyotrophic Lateral Sclerosis. *The American Journal of Pathology* **173**,

bioRxiv preprint doi: https://doi.org/10.1101/648477; this version posted May 24, 2019. The copyright holder for this preprint (which was not certified by peer review) is the author/funder. All rights reserved. No reuse allowed without permission.

182–194 (2008).

112. Zacco, E., Martin, S. R., Thorogate, R. & Pastore, A. The RNA-Recognition Motifs of TAR DNA-Binding Protein 43 May Play a Role in the Aberrant Self-Assembly of the Protein. *Frontiers in Molecular Neuroscience* **11**, (2018).

113. Sasaguri, H. *et al.* The extreme N-terminus of TDP-43 mediates the cytoplasmic aggregation of TDP-43 and associated toxicity in vivo. *Brain Res.* **1647**, 57–64 (2016).

114. Shodai, A. *et al.* Aberrant Assembly of RNA Recognition Motif 1 Links to Pathogenic Conversion of TAR DNA-binding Protein of 43 kDa (TDP-43). *Journal of Biological Chemistry* **288**, 14886–14905 (2013).

115. Neumann, M. *et al.* TDP-43-Positive White Matter Pathology in Frontotemporal Lobar Degeneration With Ubiquitin-Positive Inclusions. *Journal of Neuropathology and Experimental Neurology* **66**, 177–183 (2007).

116. Nishihira, Y. *et al.* Sporadic amyotrophic lateral sclerosis: two pathological patterns shown by analysis of distribution of TDP-43-immunoreactive neuronal and glial cytoplasmic inclusions. *Acta Neuropathologica* **116**, 169–182 (2008).

117. Zhang, H. *et al.* TDP-43-immunoreactive neuronal and glial inclusions in the neostriatum in amyotrophic lateral sclerosis with and without dementia. *Acta Neuropathologica* **115**, 115–122 (2007).

118. Serio, A. *et al.* Astrocyte pathology and the absence of non-cell autonomy in an induced pluripotent stem cell model of TDP-43 proteinopathy. *Proceedings of the National Academy of Sciences* **110**, 4697–4702 (2013).

119. Bruijn, L. I. *et al.* ALS-Linked SOD1 Mutant G85R Mediates Damage to Astrocytes and Promotes Rapidly Progressive Disease with SOD1-Containing Inclusions. *Neuron* **18**, 327–338 (1997).

120. Guo, H. Increased expression of the glial glutamate transporter EAAT2 modulates excitotoxicity and delays the onset but not the outcome of ALS in mice. *Human Molecular*

bioRxiv preprint doi: https://doi.org/10.1101/648477; this version posted May 24, 2019. The copyright holder for this preprint (which was not certified by peer review) is the author/funder. All rights reserved. No reuse allowed without permission.

Genetics **12**, 2519–2532 (2003).

121. Howland, D. S. *et al.* Focal loss of the glutamate transporter EAAT2 in a transgenic rat model of SOD1 mutant-mediated amyotrophic lateral sclerosis (ALS). *Proceedings of the National Academy of Sciences* **99**, 1604–1609 (2002).

122. Pardo, A. C. *et al.* Loss of the astrocyte glutamate transporter GLT1 modifies disease in SOD1G93A mice. *Experimental Neurology* **201**, 120–130 (2006).

123. Rothstein, J. D., Martin, L. J. & Kuncl, R. W. Decreased glutamate transport by the brain and spinal cord in amyotrophic lateral sclerosis. *N. Engl. J. Med.* **326**, 1464–1468 (1992).

124. Rothstein, J. D., Van Kammen, M., Levey, A. I., Martin, L. J. & Kuncl, R. W. Selective loss of glial glutamate transporter GLT-1 in amyotrophic lateral sclerosis. *Ann. Neurol.* **38**, 73–84 (1995).

125. Yu, J., Chau, K. F., Vodyanik, M. A., Jiang, J. & Jiang, Y. Efficient feeder-free episomal reprogramming with small molecules. *PLoS One* **6**, e17557 (2011).

126. Tank, E. M. *et al.* Abnormal RNA stability in amyotrophic lateral sclerosis. *Nat. Commun.* **9**, 2845 (2018).

127. Patro, R., Duggal, G., Love, M. I., Irizarry, R. A. & Kingsford, C. Salmon provides fast and bias-aware quantification of transcript expression. *Nat. Methods* **14**, 417–419 (2017).

128. Soneson, C., Love, M. I. & Robinson, M. D. Differential analyses for RNA-seq: transcript-level estimates improve gene-level inferences. *F1000Res.* **4**, 1521 (2015).

129. Arrasate, M., Mitra, S., Schweitzer, E. S., Segal, M. R. & Finkbeiner, S. Inclusion body formation reduces levels of mutant huntingtin and the risk of neuronal death. *Nature* **431**, 805–810 (2004).

130. Barmada, S. J. *et al.* Autophagy induction enhances TDP43 turnover and survival in neuronal ALS models. *Nat. Chem. Biol.* **10**, 677–685 (2014).

131. Saudou, F., Finkbeiner, S., Devys, D. & Greenberg, M. E. Huntingtin Acts in the Nucleus to Induce Apoptosis but Death Does Not Correlate with the Formation of Intranuclear

bioRxiv preprint doi: https://doi.org/10.1101/648477; this version posted May 24, 2019. The copyright holder for this preprint (which was not certified by peer review) is the author/funder. All rights reserved. No reuse allowed without permission.

Inclusions. *Cell* **95**, 55–66 (1998).

132. Duong, H. & Han, M. A multispectral LED array for the reduction of background autofluorescence in brain tissue. *J. Neurosci. Methods* **220**, 46–54 (2013).

bioRxiv preprint doi: https://doi.org/10.1101/648477; this version posted May 24, 2019. The copyright holder for this preprint (which was not certified by peer review) is the author/funder. All rights reserved. No reuse allowed without permission.

Figure 1.

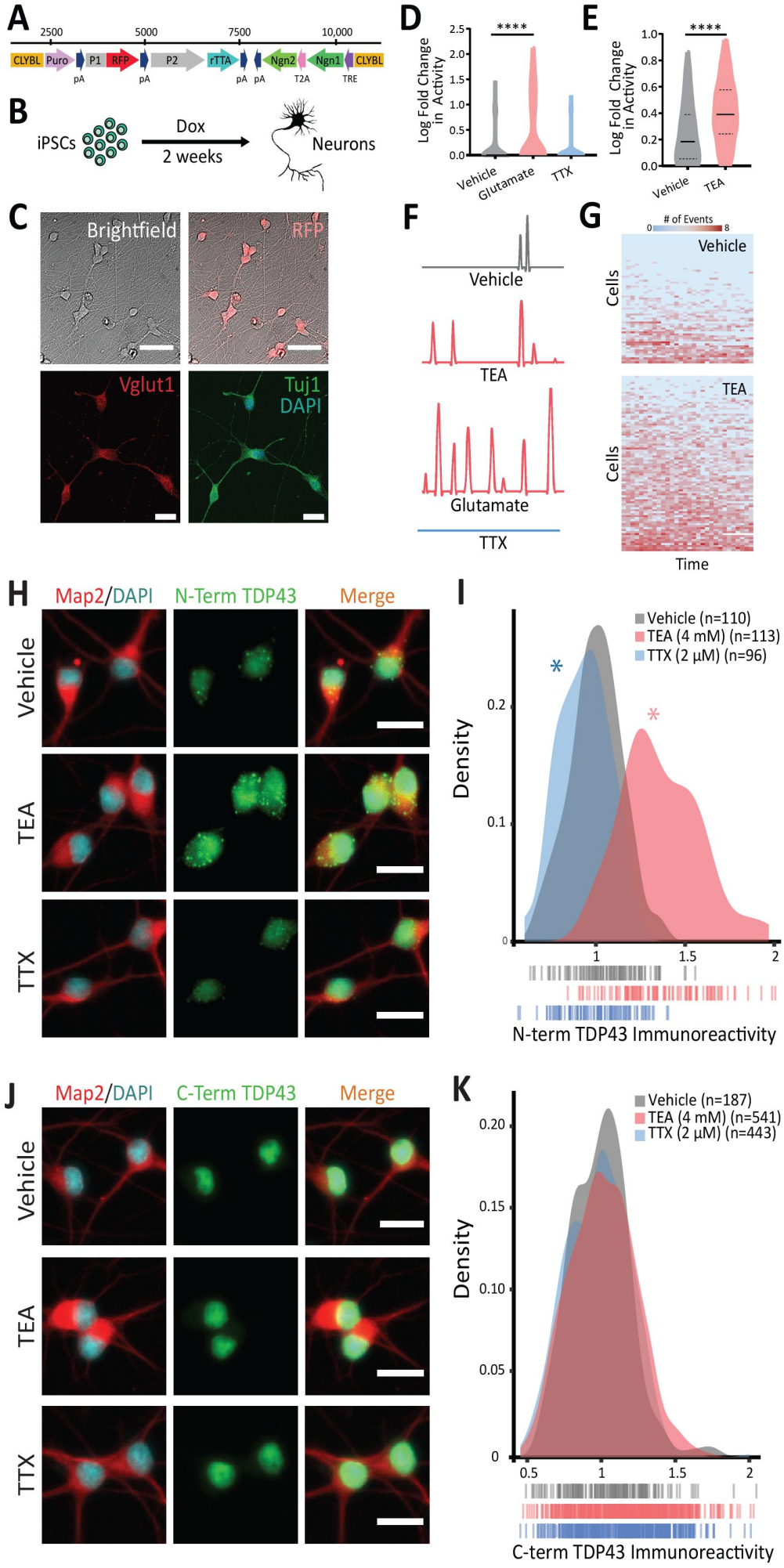

bioRxiv preprint doi: https://doi.org/10.1101/648477; this version posted May 24, 2019. The copyright holder for this preprint (which was not certified by peer review) is the author/funder. All rights reserved. No reuse allowed without permission.

Figure 2.

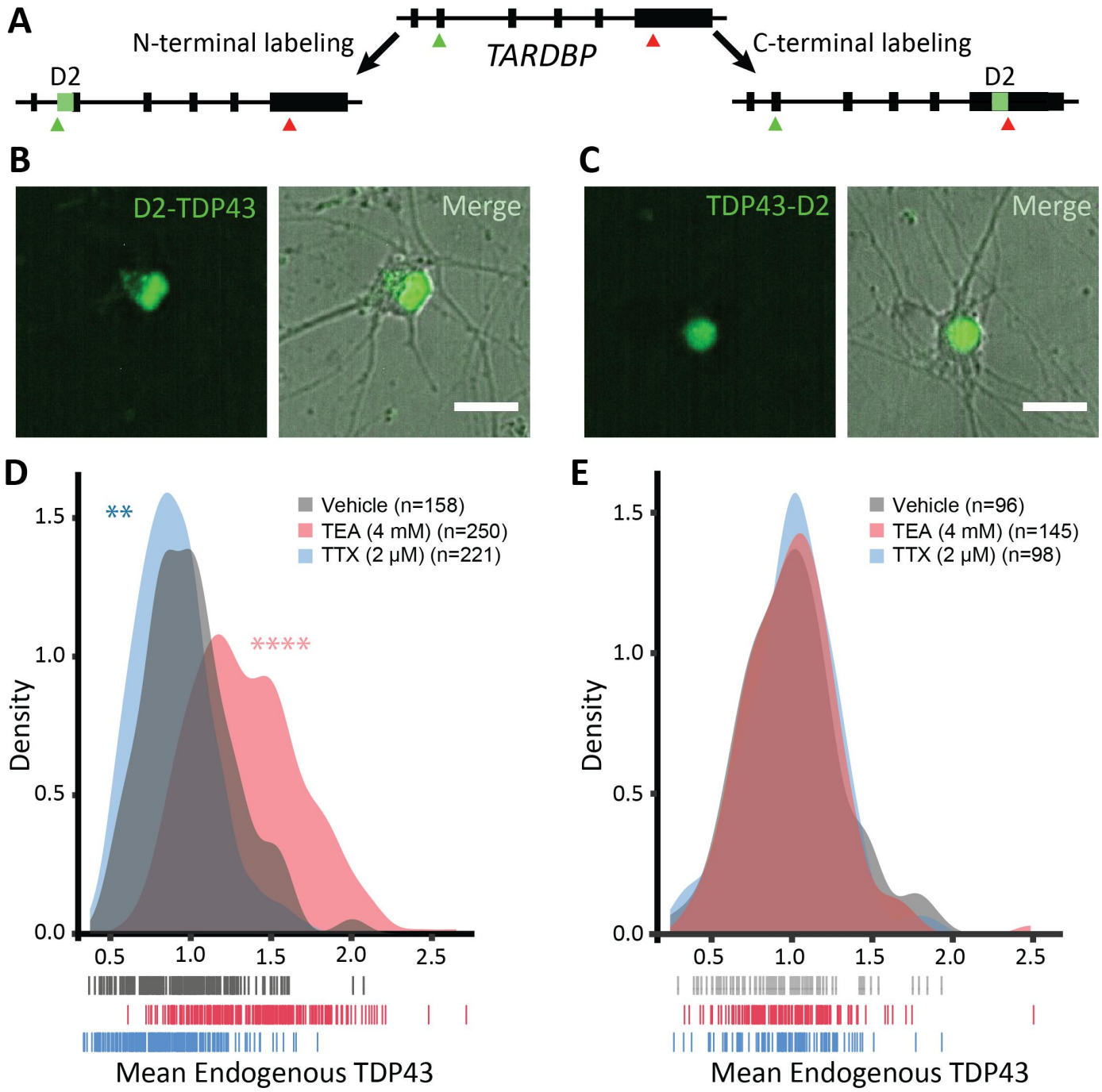

bioRxiv preprint doi: https://doi.org/10.1101/648477; this version posted May 24, 2019. The copyright holder for this preprint (which was not certified by peer review) is the author/funder. All rights reserved. No reuse allowed without permission.

Figure 3.

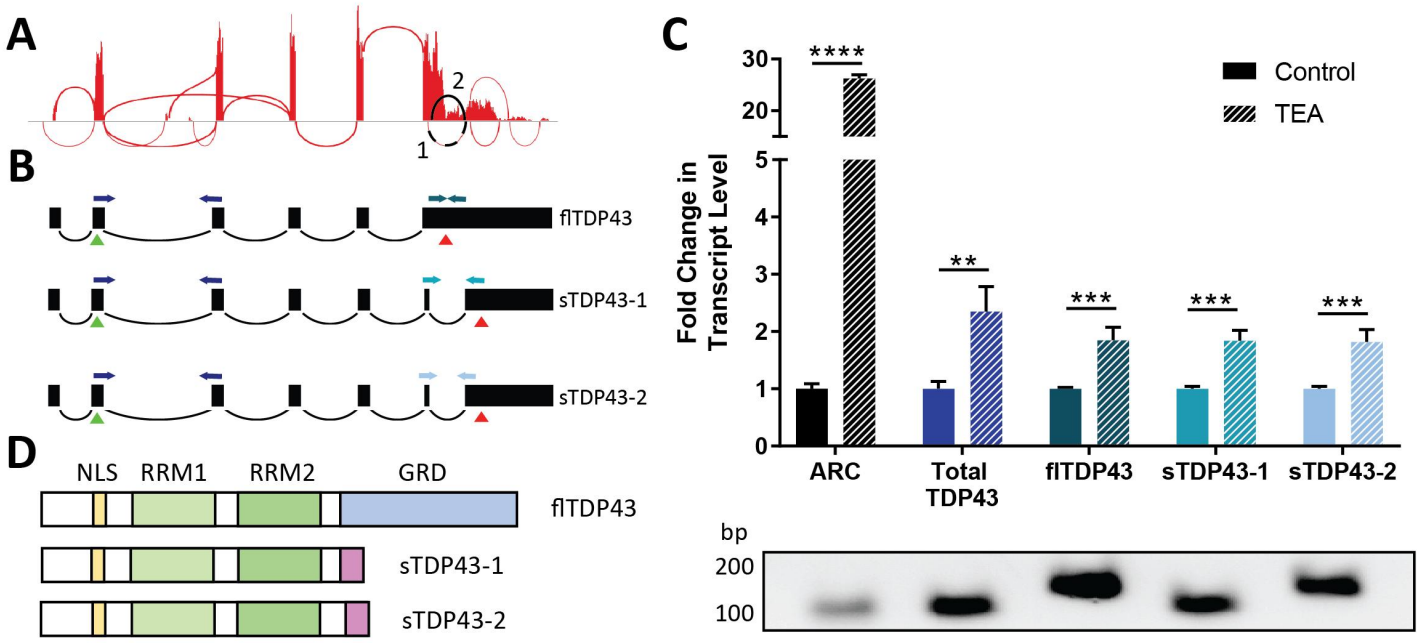

bioRxiv preprint doi: https://doi.org/10.1101/648477; this version posted May 24, 2019. The copyright holder for this preprint (which was not certified by peer review) is the author/funder. All rights reserved. No reuse allowed without permission.

Figure 4.

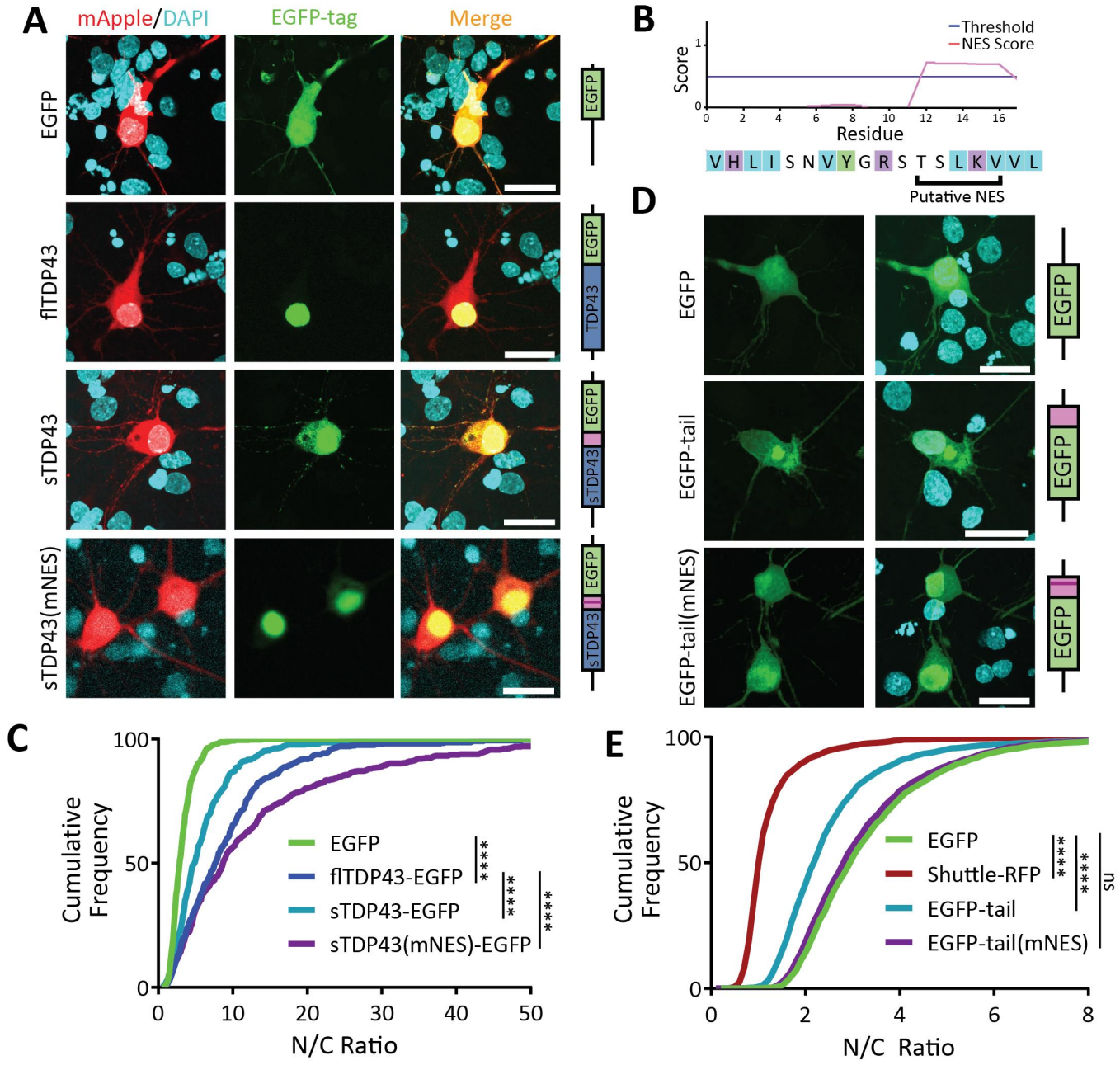

bioRxiv preprint doi: https://doi.org/10.1101/648477; this version posted May 24, 2019. The copyright holder for this preprint (which was not certified by peer review) is the author/funder. All rights reserved. No reuse allowed without permission.

Figure 5.

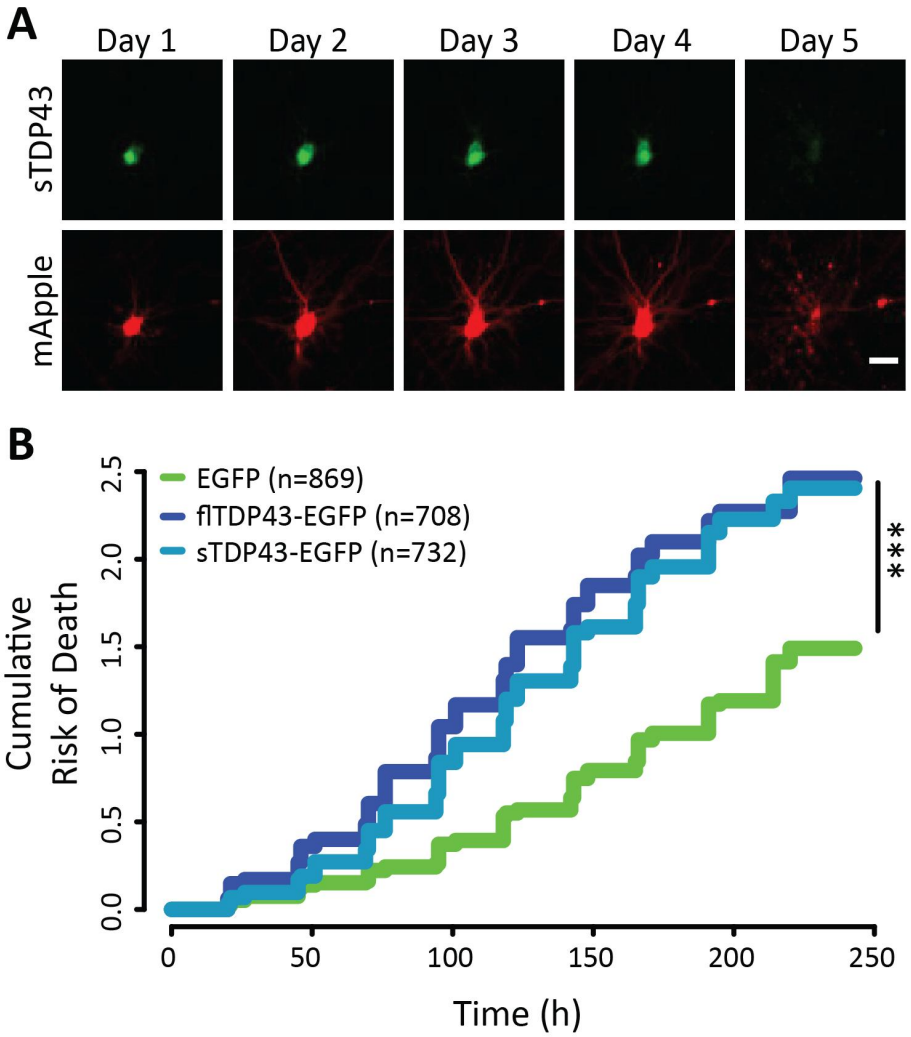

bioRxiv preprint doi: https://doi.org/10.1101/648477; this version posted May 24, 2019. The copyright holder for this preprint (which was not certified by peer review) is the author/funder. All rights reserved. No reuse allowed without permission.

Figure 6.

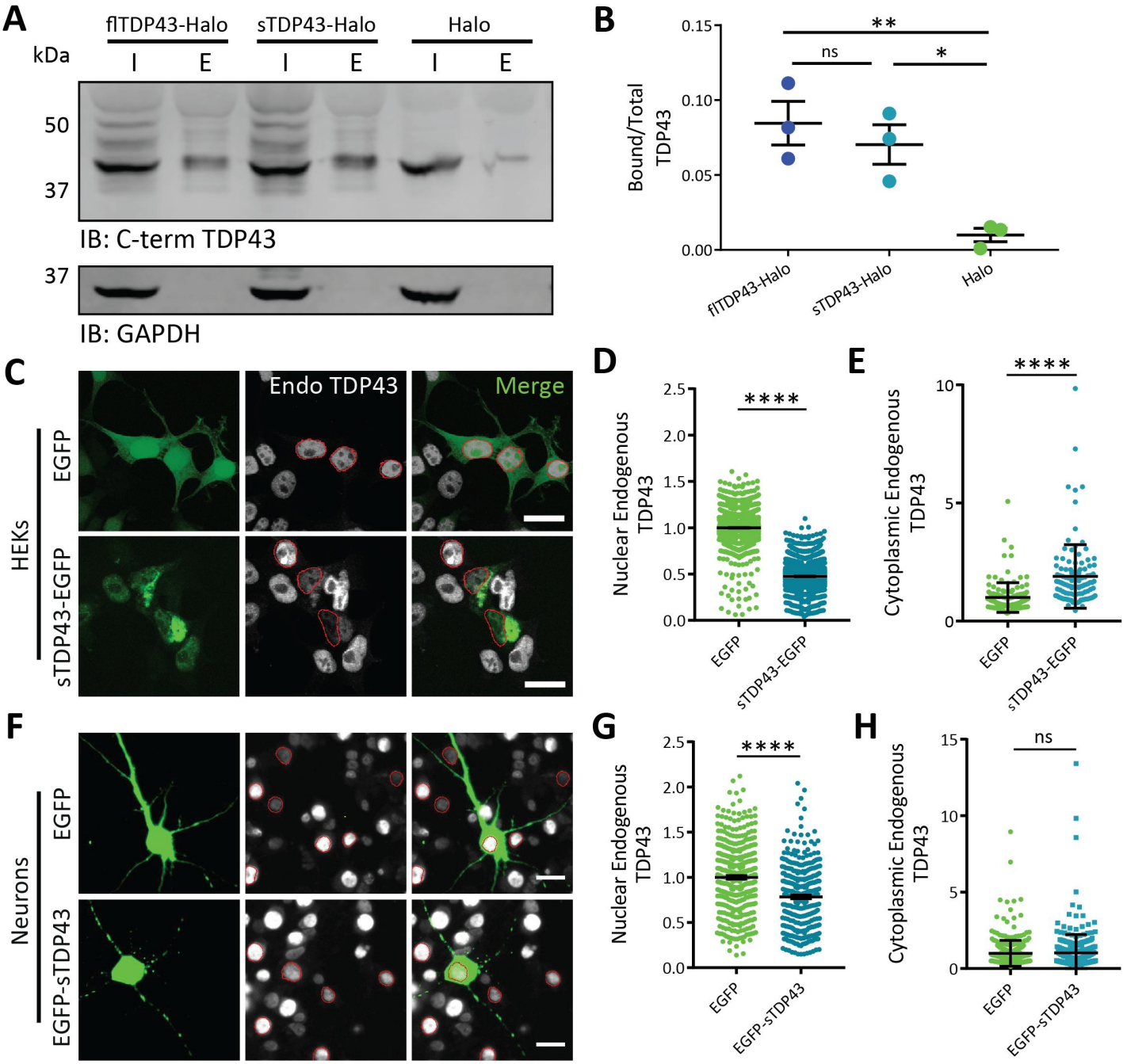

bioRxiv preprint doi: https://doi.org/10.1101/648477; this version posted May 24, 2019. The copyright holder for this preprint (which was not certified by peer review) is the author/funder. All rights reserved. No reuse allowed without permission.

Figure 7.

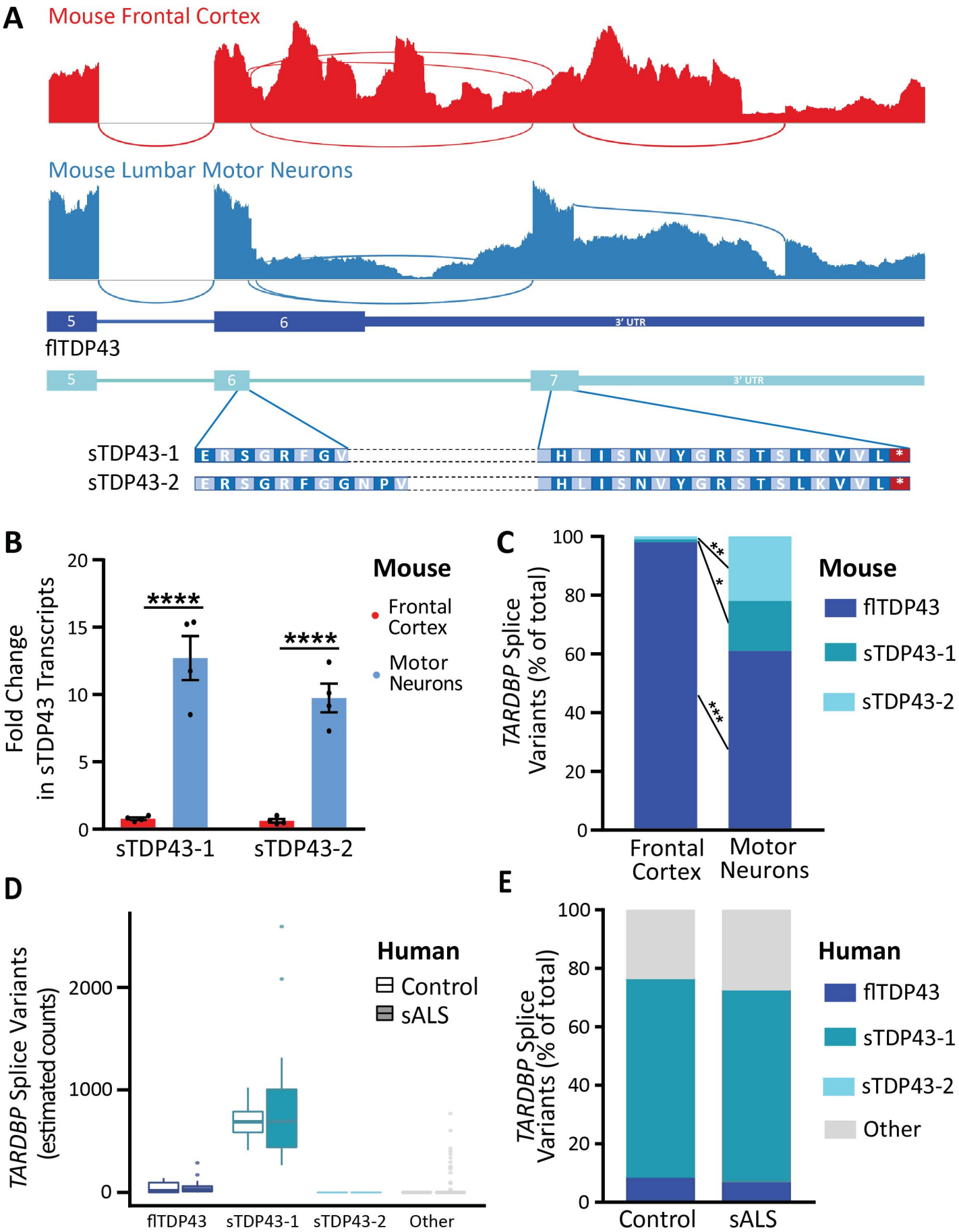

bioRxiv preprint doi: https://doi.org/10.1101/648477; this version posted May 24, 2019. The copyright holder for this preprint (which was not certified by peer review) is the author/funder. All rights reserved. No reuse allowed without permission.
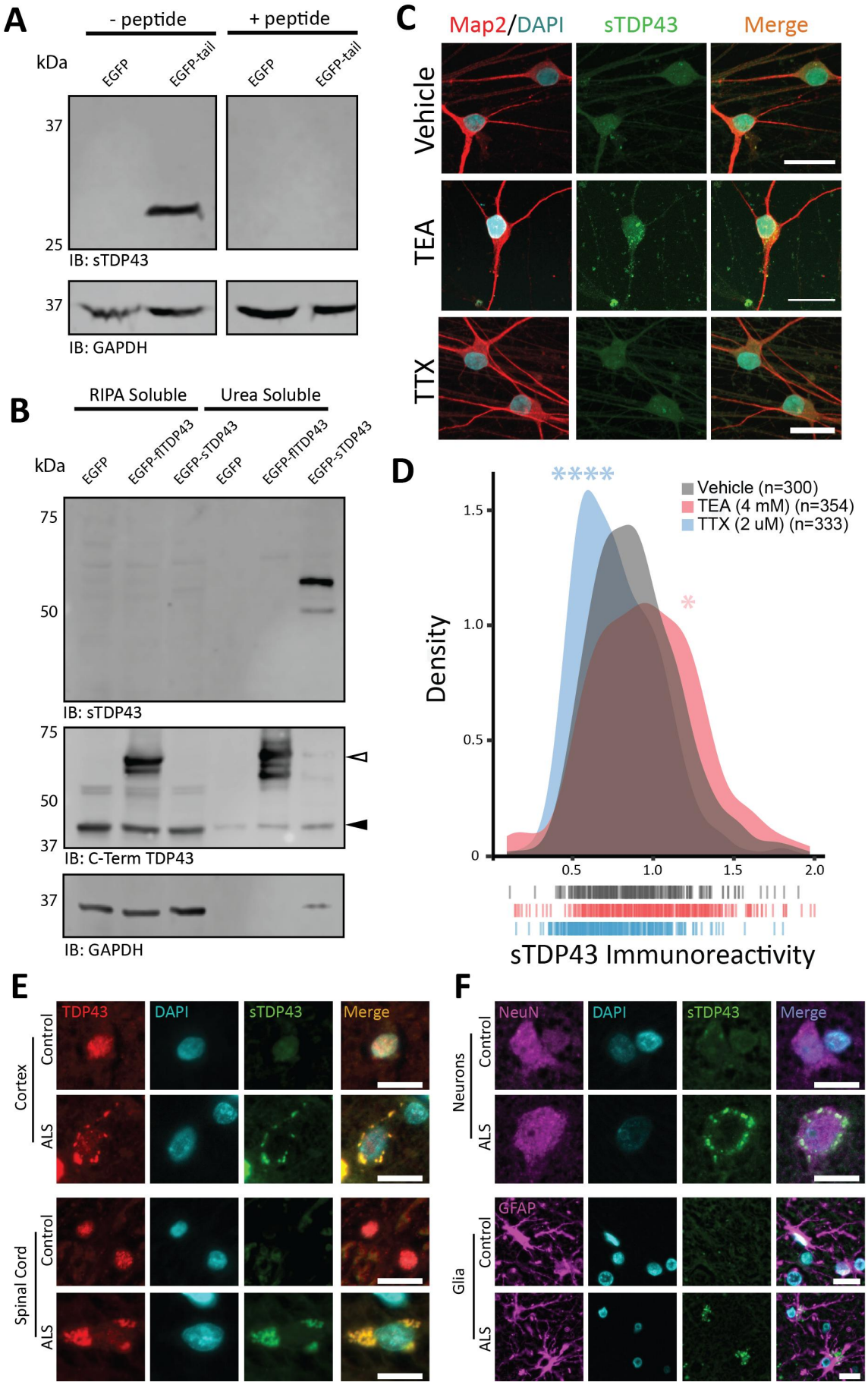
Figure 8.